Experimental study of the heat transfer of single-jet impingement cooling onto a large heated plate near industrial conditions

A. v. s. Oliveira, D. Maréchal, J.-L. Borean, Vincent Schick, Julien Teixeira, S. Denis, Michel Gradeck

Experimental study of the heat transfer of single-jet impingement cooling onto a large heated plate near industrial conditions

A. V. S. Oliveira[a,b,c], D. Maréchal[a], J. L. Borean[d], V. Schick[b], J. Teixeira[c,e], S. Denis[c,e], M. Gradeck[b,*]

[a] *IRT M2P, 4 rue Augustin Fresnel 57070 Metz, France*
[b] *Université de Lorraine, CNRS, LEMTA, F-54000 Nancy, France*
[c] *Université de Lorraine, CNRS, IJL, F-54000 Nancy, France*
[d] *ArcelorMittal Global Research and Development, Voie Romaine, BP 30320, F-57283 Maizières-lès-Metz Cedex, France*
[e] *Laboratory of Excellence "Design of Alloy Metals for Low-mass Structures" (DAMAS), Univ. Lorraine, Nancy, France*

Abstract

Jet impingement cooling has been intensively studied in the past by many authors because of its important application in the metallurgical industry; however, most of the experiments in the literature are at laboratory scale and, in some cases, not near industrial conditions. In this study, we performed cooling experiments near industrial conditions in a new experimental apparatus with a large nickel plate as test sample, which was heated until 850 °C before being cooled by a single circular water jet. Five experimental results are presented with different jet Reynolds numbers, from 9,800 to 120,000, obtained by varying the water flow rate and the nozzle diameter. The presented results are: temperature evolutions during cooling, dissipated heat flux (estimated by solving a 2D inverse heat conduction problem), transverse heat flux at the heat-exchanging surface, and the characteristics (position and velocity) of the rewetting and maximum cooling rate fronts. The increase in the jet Reynolds number increased slightly the heat flux at the stagnation zone, but increased it substantially for positions farther from the impact location. The transverse heat flux increased with the passage of the rewetting front and then decreased, and its magnitude was practically the same regardless of the jet Reynolds number. The change in the nozzle diameter did not affect significantly the heat transfer nor the rewetting front growth, although the heat dissipation was slightly higher with the smaller nozzle, possibly because of the higher jet impact velocity. Finally, we compared the present results with some found in the literature in similar conditions, showing that laboratory experiments are valuable to provide detailed information, especially near the stagnation zone, but large-scale experiments allow obtaining macroscale data of the cooling process.

Keywords:
Quenching, Inverse problem, Heat conduction, Boiling, Film boiling, Critical heat flux, Rewetting

Nomenclature

Roman letters			
ω_i	Fourier's i-th eigenvalue	a	thermal diffusivity
A	power-law coefficient	b	power-law exponent
		c_p	specific heat

*Corresponding author
Email address: michel.gradeck@univ-lorraine.fr (M. Gradeck)

d	diameter
h	height
I	pixel intensity
i	Fourier harmonic
L	length
n_{fts}	number of future time steps
p	Laplace variable
Q	volumetric flow rate
r	position
Re	Reynolds number
T	temperature
t	time
TC	thermocouple
v	velocity
X	thermal impedance
x, y, z	coordinates
Z	Solution of the inverse Laplace transform

Greek letters

λ	thermal conductivity
ν	kinematic viscosity
ρ	density
σ	standard deviation
τ	response time
θ	temperature difference
φ	heat flux

Subscripts

φ	heat flux
0	initial
c	characteristic
j	jet
k	time step
max	maximum
MCR	maximum cooling rate
MHF	maximum heat flux
n	nozzle
rew	rewetting
s	surface
w	wall

Superscripts

˜	Fourier domain
–	Laplace domain

1. Introduction

Many engineering applications demand the use of very efficient heat dissipation methods, and the ones that allow extracting the highest heat fluxes involve liquid-vapor phase change, like nucleate boiling and high-temperature cooling with falling films, sprays or jets impingement. More precisely, water is the most used working fluid because of its unique properties that results in the most elevated heat flux exchanges observed in the literature (above 1 MW/m^2). We find many examples of applications in nuclear engineering [1, 2], electronics [3, 4], or refrigeration [5], as well as attempts to increase the heat dissipation [6, 7]. In metallurgy, we find another classical use of high dissipation methods: water quenching, which consists of cooling rapidly metallic parts initially at very high temperatures. This process can be performed by immersing the part in a liquid pool or by jet or spray impingement onto the surface. Pool immersion is usually less expensive and may be appropriate for simpler geometries, large parts and large production volumes. Meanwhile, sprays are, for instance, recommended for complex-shaped parts or when higher heat fluxes are necessary, although ensuring homogenized heat dissipation is not simple [8].

Jet impingement, in turn, is largely used for fast cooling of metallic plates after hot rolling and, therefore, it motivated several studies about heat transfer and wall rewetting dynamics. Agrawal et al. [9] tested two different nozzle types, one sharp-edged and the other tube-type, to generate the water jet impingement onto a stainless steel thin sheet. They observed that the cooling is unaffected by the nozzle type at the stagnation point, but the rewetting temperature and wetting velocity are higher when using the tube-type nozzle. Nallathambi and Specht [10] tested the cooling of a vertical rectangular nickel plate (200 x 110 x 2 mm^3) using an array of eight water jets. They observed the increase in the jets velocity increased the maximum heat flux near the impact location, but reduced it far from the impact. Gradeck et al. [11] compared the heat transfer of jet impingement with water and an oil-in-water emulsion (simulating contaminated cooling water) onto a nickel plate (175 mm diameter, 5 mm thickness). They observed that the water contamination with oil made the rewetting front propagate faster, hence improving the heat transfer far from the impact location. Gomez et al. [12] tested water jet impingement cooling of a AISI304 stainless steel plate (50 x 50 x 10 mm^3) for different initial wall temperature and liquid subcooling. They demonstrated that both parameters affect substantially the boiling curve and the rewetting temperature. Liquid subcooling also played an important role on the jet cooling of a downward surface in the Hammad et al. investigation [13], especially on the rewetting front spreading time.

Table 1 presents other experimental studies of hot-metal cooling using water jet impingement, considering only upward surface cooling. Data of the present study are also included in the end of the table for comparison. This list is not exhaustive, but demonstrates typical scales of experimental campaigns available in the literature. Most of the studies mentioned in the previous paragraph and presented in the table are for relatively small specimens, which are far from industrial scale. In fact, we can cite few studies using larger cooled parts. Lee et al. [14] tested a 300 x 200 x 20 mm^3 AISI304 stainless steel plate and they could identify the different heat transfer regimes and reconstruct the 2D heat flux dissipation with the use of 22 thermocouples. Later, the same authors performed similar experiments but with two interacting water jets [15], identifying the merging front where the heat transfer coefficient is enhanced and the rewetting front spreads faster. Wang et al. [16] studied the cooling of a 410 x 200 x 25 mm^3 AISI304L plate using eight in-line impinging jets and they observed that the water flow rate had negligible effect on the heat transfer coefficient within 70 mm from the stagnation line. The largest jet-impinged samples found in the literature by the present authors were tested by Nobari et al [17]. They used High Strength Low Alloy (HSLA) steel plates larger than 400 mm (up to 600 mm length) and with 6.6 mm thickness, and tested both circular and planar jets. They developed a model for the transient cooling, without considering the latent heat due to phase transformation, and obtained satisfactory results of tracing boiling curves departing from the film boiling regime at different locations on the plate surface.

Although we observe an increase of experimental campaigns aiming at better reproducing industrial cooling conditions, most of the past works use samples far from the industrial scale. This motivated the construction of a near-industrial scale experimental bench at the IRT M2P (Institut de Recherche Technologique: Matériaux, Métallurgie, Procédés), capable of performing cooling experiments with settings close to industrial conditions: static or moving (rotation, translation) pieces (plates, tubes, blooms or billets) cooled with industrial devices with high flow rates. This paper presents experimental results of cooling experiments carried out with this new test apparatus with a single static jet impinging onto a large heated plate. After introducing a brief theory review of jet impingement

Table 1: Experimental studies of hot-metal cooling with water jet impingement.

Authors	Year	Specimen material	Specimen dimensions [mm]	$T_{w,0}$ [°C]	T_j [°C]	Nozzle size[a] [mm]	Water jet size[b] [mm]	v_j [m/s]	Q_j [l/min]	$\varphi_{w,MHF}$ [MW/m^2]	$T_{w,rew}$ [°C]	v_{rew} [mm/s]	Δt_{rew} [s]
Agrawal et al. [18, 19]	2012, 2013	AISI316	130 x 38 x 0.25	800	22	∅2.5 - ∅4.8	-	0.9 - 8.4	0.5 - 4.75	1.1 - 2.5	754 - 800	8 - 100	-
Gomez et al. [12]	2021	AISI304	50 x 50 x 10	250 - 550	25 - 97	∅9	-	3.1	-	0.5 - 4.2	300 - 400	-	-
Karwa and Stephan [20]	2013	AISI314	∅50 x 20	885 - 900	13 - 40	∅3	∅2.9	2.5 - 10	-	6.2 - 9.5	400 - 640	0 - 90 [c]	-
Lee et al. [14]	2017	AISI304	300 x 200 x 20	900	15	∅3	-	5.4 [d]	2.3	1 - 6.5	600 - 850	-	-
Leocadio et al. [21]	2009	AISI304	150 x 150 x 10	600 - 900	22	∅10	∅6.8	2.7	6	2.2 - 2.9	-	-	-
Leocadio et al. [22]	2018	AISI304	50 x 50 x 10	300 - 900	20 - 70	∅9.7	∅8	1 - 3	-	5 - 6.5	450 - 840	-	0.02 - 1
Nobari et al. [17]	2016	HSLA steel	600 x 430 x 6.6	720	10 - 40	30 x 3	30 x 3	2.3 - 4.8	100 - 250	4 - 16	-	-	-
Nobari et al. [17]	2016	HSLA steel	430 x 400 x 6.6	720	10 - 40	∅19	∅19	1.7 - 3.0	15 - 45	3 - 13	-	-	-
Robidou et al. [23]	2002	Ni plating	80 x 10 x 5.8	100 - 500	83 - 93	-	9 x 1	0.7 - 0.8	-	1.5 - 4.2	180 - 450	-	-
Wang et al. [24]	2016	AISI304L	150 x 80 x 20	200 - 900	10 - 40	-	4	2 - 8	-	1 - 8	200 - 850	5 - 90	0.2 - 8
Present study	2021	Ni-201	800 x 500 x 20	844 - 854	25	∅8 - ∅10	∅7.8 - ∅10	1.1 - 10.7	3.2 - 50	1 - 5.1	580 - 850	0.3 - 102	0 - 110

[a] This is the size of the nozzle generating the water jet, which may differ significantly from the water jet size because of the cross-sectional area reduction during the fall.

[b] If the nozzle generates a circular water jet, this dimension is d_j.

[c] In their paper, they present this range but in m/s, although the evolution in the rewetting front position suggests that these values are actually in mm/s.

[d] Estimated using the flow rate and nozzle size information.

and the experimental apparatus, we present and discuss the test results for different Reynolds number by varying the water flow rate and the nozzle diameter, including the samples temperature evolution at several locations and the dissipated heat flux by the impinged jet, which was estimated solving a two-dimensional inverse heat conduction problem. We also present results for the transverse heat flux at the surface and the evolution of the rewetting and maximum cooling rate fronts, which are defined in the next sections. These results were compared with other experiments found in the literature.

2. Jet impingement: definitions and mechanisms

As already demonstrated, there is a large literature about water jet impingement heat transfer, which means that many mechanisms have already been described. However, some processes or events are often defined differently in the literature, and, for this reason, we established in the list below some terms and definitions used in this paper, mostly based on those presented by Leocadio et al. [22] and Gomez et al. [12]:

- *Cooling process*: the term used for sample temperature decrease by jet impingement in our experiments, which is sometimes called simply as *cooling*. We did not refer to our tests as *quenching*, which is a transient process of fast cooling of hot parts aiming specific material's microstructures and properties, because we are not considering the metallurgical characteristics of the part after the cooling experiment;
- *Stagnation zone*: test plate area directly below the nozzle where normal impact of the jet occurs, hence the local fluid velocity is very low or nearly zero;
- *Film boiling regime*: heat transfer process where there is a stable vapor layer between the heated surface and the liquid;
- *Boiling curve*: representation of the dissipated heat flux (φ_w) as a function of the local wall superheat, which is the difference between the wall and jet temperatures (T_w and T_j, respectively);
- *Maximum heat flux (MHF)*: point where the heat transfer between the wall and the jet is maximal;
- *Maximum cooling rate (MCR)*: point where the cooling rate at a given position is maximal;
- *Wall rewetting*: phenomenon of departure from film boiling, i.e. when the vapor layer between the wall and the liquid starts to collapse and transition boiling takes place, so both wet and dry regions are present in this process [22];
- *Rewetting front*: line defining the limit between film and transition boiling regimes;
- *Rewetting temperature* ($T_{w,rew}$): temperature at the rewetting front location;
- *Rewetting delay* (Δt_{rew}): time between the start of the jet impingement and the moment when the rewetting front reaches a given location, like a temperature measurement position;
- *Rewetting front velocity* (v_{rew}): the velocity of the rewetting front at a given position or time.

In a single-jet impingement cooling of a static plate, the heated plate is initially at a high temperature (about 900 °C in industrial conditions). In the moment the jet impacts onto the surface, the heat transfer occurs in the film boiling regime, which can last much less than one second at the stagnation zone because the wall is rapidly rewetted there [22]. For this reason, this moment is usually not observed with thermocouple measurements. Then, the rewetting front advances progressively outward the impact point and several heat transfer processes are observed (Fig. 1). From the stagnation zone until a point where the surface temperature is not high enough to generate bubbles, the wall is wet and single-phase heat transfer is predominant. Still in the wet region but at slightly higher wall temperatures (normally farther from the stagnation zone), bubbles are generated so nucleate boiling occurs up to a point where the temperature is high enough to permit intermittent wall dry-out. After this point, there is the rewetting region where transition boiling is the characteristic heat transfer process. Between transition and nucleate boiling regions is where we find the maximum heat dissipation by the jet impingement. The other limit of the rewetting region is given by the rewetting front position, which also delimits the beginning of the film boiling region where the surface temperature is sufficiently high to impede wall-liquid contact, resulting in much lower heat transfer capacity. Because liquid is constantly injected onto the surface, a liquid sheet is lifted in the film boiling regime and breaks up due to hydrodynamic instabilities, generating digitations and droplets that bounce and slip over the heated surface (still in the film boiling regime). Karwa and Stephan [20] presented these hydraulic phenomena with more details in their experimental observations. These regions and lamella formation are as well present with jet impingement onto downward surfaces [13], rotating cylinders [25] or falling liquid films [2].

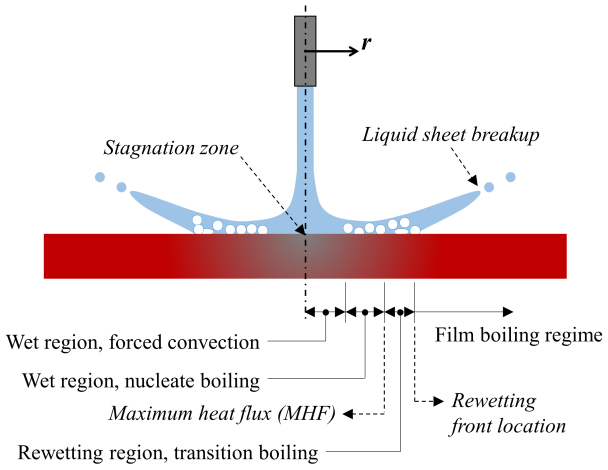

Figure 1: Illustration of jet impingement onto a heated surface and the different heat transfer phenomena involved during the cooling.

3. Experimental apparatus and test procedure

Figure 2 presents a photograph of the cooling experiment apparatus installed at IRT M2P. The entire installation measures 7 x 3 x 5 m^3 and is mainly composed of a cooling chamber, a furnace, a compressed air tank and a pre-heated water tank. The cooling chamber allows testing plate samples as large as 1000 mm long and 500 mm large and rotating cylindrical parts with diameters up to 250 mm. The water injection system, which can be one or more nozzles or a spray ring for cylinders, can be either static or mobile, moving at velocities up to 600 mm/s. The test samples can be instrumented with up to 15 thermocouples, whose signal is transmitted wireless by a data acquisition

system protected inside a housing to the collection system that transfers the data to a computer. A high-definition camera was installed at the cooling chamber's ceiling to visualize and register images of the experiments. The furnace heats up the test sample to 900 °C in a controlled nitrogen environment to avoid surface oxidation before the cooling experiment. Water injection occurs through a hydraulic circuit starting from the water tank (2000 liters), which has a pre-heating system to control the liquid temperature, pressurized by the compressed air stored in a 2500-liter tank.

Figure 2: Photograph of the large-scale cooling experimental bench: 1) cooling chamber; 2) furnace; 3) compressed air tank; 4) pre-heated water tank.

In this study, we present experimental results of static single-jet impingement cooling of a heated plate, which was the first complete experimental campaign using this experimental bench. Figure 3 presents a schematic drawing of the hydraulic circuit, which uses flowmeters, pressure transducers and thermocouples to measure the flow rate, injection pressure and liquid temperature during the cooling experiment. The use of two flowmeters, one for lower flow rates and another for higher values, is necessary to allow testing a large flow rate range always with appropriate accuracy. The test sample, a 802 x 500 x 19.5 mm^3 nickel plate (Ni-201) with average surface roughness between 2 and 8 μm, was instrumented with 15 type-N thermocouples (1 mm diameter, sheathed and ungrounded), which were inserted through the bottom surface and fixed so their tip is only about 0.6 mm below the impinged surface, without thermal paste. For the present experiments, the jet nozzle was located between 40 and 100 mm above the heated plate surface, just above the 7^{th} thermocouple (TC7) at $x = 370$ mm, with the water temperature fixed at about 25 °C. Also, the tested water flow rates varied between 3.2 and 50 l/min and we tested two different nozzle diameters (8 and 10 mm), which give jet impact velocities between 1.1 and 10.7 m/s and jet impact Reynolds numbers Re_j between 9,800 and 120,000, Re_j being defined by:

$$Re_j = \frac{v_j d_j}{\nu_j} \tag{1}$$

where v_j and d_j are, respectively, the jet normal velocity and diameter at impact, while ν_j is the kinematic viscosity of water. The data acquisition system recorded the temperature measurements at a sampling rate of 50 Hz.

Table 2 introduces the experimental conditions of the tests used in this study. More precisely, we present: the jet temperature T_j, the nozzle diameter d_n and height from the heated plate h_n, the flow rate Q_j, the jet diameter at impact d_j (estimated by mass balance from the nozzle to the heated surface), the jet velocity at impact v_j (estimated

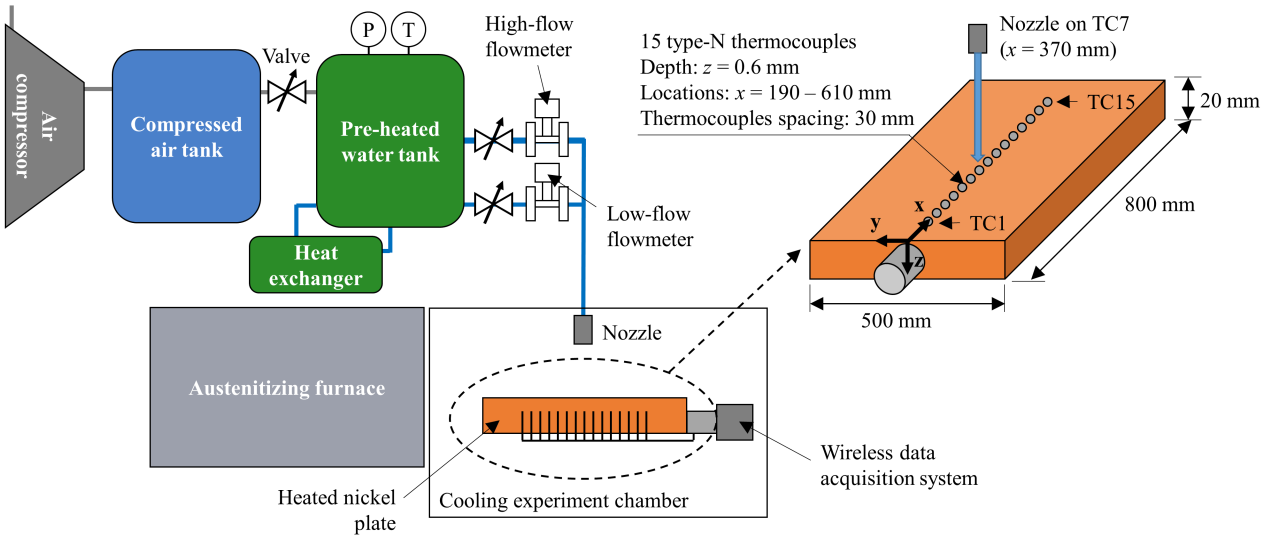

Figure 3: Schematic drawing of the hydraulic circuit for the water injection.

using Bernoulli's equation), the jet Reynolds number Re_j, and the initial wall temperature $T_{w,0}$, whose value is the mean of all the thermocouples' measurements (the uncertainty comprises the maximum and the minimum values found before the cooling experiment). As we can see, the test conditions allow us to evaluate the Reynolds number effect by varying the flow rate and the nozzle diameter. The initial wall temperature is almost the same for all the experiments, around 850 °C, and the plate temperature was almost homogeneous before starting the cooling experiments, generally varying by less than 6 °C. We also present in Table 2 the temperature derivative threshold $(\partial T_w/\partial t)_{rew}$ used to identify the rewetting front position, as discussed in section 4.2.

Table 2: Experimental conditions for each test and their temperature derivative threshold for the rewetting front position estimation.

Test	T_j **[°C]**	d_n **[mm]**	h_n **[mm]**	Q_j **[l/min]**	d_j **[mm]**	v_j **[m/s]**	Re_j **[-]**	$T_{w,0}$ **[°C]**	$(\partial T_w/\partial t)_{rew}$ **[°C/s]**
1	25	10	40	3.2	7.8	1.1	9,800	844 ± 6	-2.9
2	25	10	40	9.4	9.6	2.2	23,500	844 ± 4	-2.7
3	27	10	100	20	9.7	4.5	51,300	850 ± 3	-3.5
4	25	10	100	50	10.0	10.7	120,000	844 ± 6	-6.3
5	24	8	100	20	7.9	6.8	59,000	846 ± 6	-2.6

The tests were performed according to the following steps:

1. The instrumented sample was heated in the furnace until reaching a temperature of 900 °C, this temperature is maintained for at least one hour. The data acquisition is started at this step;
2. Once all the experimental conditions were set and stable (injection pressure and water temperature), the camera started recording and the heated sample was removed from the furnace, brought to the cooling chamber and placed on four border supports, with the aid of automatic motion devices;

3. The jet nozzle is at first located over the sample's supporting side-bar. The water injection is started and is maintained at this position for a few seconds until the water flow is stabilized. This waiting time until starting the cooling experiment results in a sample temperature decrease of about 50 °C due to heat loss to the environment;
4. When the test conditions are reached and stable, the nozzle is automatically and rapidly moved to the center of the heated plate. At this point the cooling experiment starts effectively and lasts for two minutes.

4. Data reduction and uncertainty analysis

The measurement of the liquid pressure, temperature and flow rate, as well as the different sample temperatures, were obtained directly from their respective measurement instrument and the data acquisition system. With the temperature measurements, we estimated the dissipated and transverse heat fluxes solving a two-dimensional inverse heat conduction problem, while the rewetting front characteristics (position and velocity) were obtained from thermocouples acquisitions and verified by image processing. We present more details of both steps in the next sub-sections, ending with a summary of the involved uncertainties.

4.1. Heat flux estimation

The present problem was modeled as a two-dimensional domain (xz-plane according to the coordinates in Figure 3, the plane where the thermocouples were placed), assuming the heat exchange in the y-direction is negligible over this plane (due to symmetry), as well as the term $\partial^2 T/\partial y^2$ in the heat equation compared with the other spatial second derivatives. Although our test case is actually a three-dimensional Cartesian problem, our 2D inverse method performed well for the heat flux estimate using data from a 3D numerical simulation, estimating the imposed heat flux on the simulation with errors smaller than 1%. Furthermore, we considered the nickel thermophysical properties constant with temperature ($\rho = 8700$ kg.m^{-3}, $\lambda = 52$ W.m^{-2}.K^{-1}, and $c_p = 525$ J.kg^{-1}.K^{-1}, which are, respectively, the density, thermal conductivity and specific heat). Therefore, the heat equation for the present case is:

$$\frac{\partial^2 \theta}{\partial x^2} + \frac{\partial^2 \theta}{\partial z^2} = \frac{1}{a}\frac{\partial \theta}{\partial t} \tag{2}$$

where $\theta = T - T_0$ is the difference between the local temperature T and the plate initial temperature T_0 (assumed constant and uniform for all the domain), t is the time, and $a = \lambda \rho^{-1} c_p^{-1}$ is the thermal diffusivity. We use both the Laplace and Fourier transforms to solve this equation [26]. After the Laplace transform, p being the Laplace variable and $\overline{\theta}$ the temperature in the Laplace domain, the heat equation becomes:

$$\frac{\partial^2 \overline{\theta}}{\partial x^2} + \frac{\partial^2 \overline{\theta}}{\partial z^2} = \frac{p}{a}\overline{\theta} \tag{3}$$

Next, the Fourier cosine transform is applied on the x-coordinate (appropriate when considering both boundaries in the x-direction as insulated [27]) and we find an ordinary differential equation for $\widetilde{\overline{\theta}}$, which is the temperature in both Laplace and Fourier domains:

$$\frac{\partial^2 \widetilde{\overline{\theta}}}{\partial z^2} - \omega_i^2 \widetilde{\overline{\theta}} = \frac{p}{a}\widetilde{\overline{\theta}} \tag{4}$$

where $\omega_i = i\pi/L$, with L being the plate length (in the x-direction) and i being a non-negative integer (i = 0, 1, 2,...). The solution for this equation, already considering both boundary conditions at $z = 0$ (heat flux $\varphi_w(x,t)$) and $z = e$ (insulated surface, as the heat loss here is very low compared to the other surface), e being the plate thickness, is the following expression:

$$\widetilde{\overline{\theta}}(z,i,p) = \frac{\widetilde{\overline{\varphi}}_w(i,p)}{\lambda} \frac{1}{\sqrt{\omega_i^2 + \frac{p}{a}}} \left[\frac{\cosh\left(z\sqrt{\omega_i^2 + \frac{p}{a}}\right)}{\tanh\left(e\sqrt{\omega_i^2 + \frac{p}{a}}\right)} - \sinh\left(z\sqrt{\omega_i^2 + \frac{p}{a}}\right) \right] \tag{5}$$

where $\widetilde{\overline{\varphi}}_w$ is the heat flux at z = 0 in the Laplace and Fourier domains. We can do the inverse Laplace transform using its convolution and shift properties and find the solution for the temperature only in the Fourier domain $\widetilde{\theta}$, i.e.:

$$\widetilde{\theta}(z,i,t) = \frac{1}{\lambda} \int_0^t \widetilde{\varphi}_w(i,t) e^{-\omega_i^2 a(t-\tau)} Z(z,t-\tau) d\tau \tag{6}$$

$Z(z,t)$ being the solution of the inverse Laplace transform of the function $\overline{Z}(z,p)$, which is given by:

$$\overline{Z}(z,p) = \frac{1}{\sqrt{\frac{p}{a}}} \left[\frac{\cosh\left(z\sqrt{\frac{p}{a}}\right)}{\tanh\left(e\sqrt{\frac{p}{a}}\right)} - \sinh\left(z\sqrt{\frac{p}{a}}\right) \right] \tag{7}$$

This solution is not easily found analytically and, for this reason, we used the Stehfest algorithm [28] to calculate $Z(z,t)$ using Eq. 7. We can consider the heat flux harmonic $\widetilde{\varphi}_w(i,t)$ constant by parts, similarly to the Duhamel's theorem [26], split the integral into a summation for each part and obtain the following expression:

$$\widetilde{\theta}(z,i,t_k) = \sum_{m=0}^{k-1} X(z,t_k - t_m) \widetilde{\varphi}_w(i,t_k) \tag{8}$$

where:

$$X(z,t_k) = -\frac{1}{\lambda} \int_{t_k}^{t_{k+1}} Z(z,\tau) d\tau \tag{9}$$

In the present study, the temperature harmonic $\widetilde{\theta}$ is known after finding each Fourier harmonic using the measurements from the 15 thermocouples at each instant, while $Z(z,t)$ is calculated using the aforementioned Stehfest algorithm on Eq. 7. Equation 8 shows that estimating a heat flux value in the Fourier domain ($\widetilde{\varphi}_w(i,t_{k-1})$) requires knowing the current and past temperature measurements (from $\widetilde{\theta}(z,i,t_0)$ to $\widetilde{\theta}(z,i,t_k)$) and past heat flux estimates (from $\widetilde{\varphi}_w(i,t_0)$ to $\widetilde{\varphi}_w(i,t_{k-2})$). This inversion of Eq. 8 diverges very rapidly because of the thermocouple noise amplification; this is typical in inverse methods because it is an ill-posed problem. Regularization methods are capable to overcome this issue and, in this study, we used Beck's function specification method [29], which consists of a temperature measurement filtering using a functional for estimating future heat fluxes with Eq. 8. We used the simplest functional of assuming that the n_{fts} future heat fluxes are equal to heat flux being currently estimated, so we obtain a system of equations to estimate $\widetilde{\varphi}_w(i,t_{k-1})$, which is solved using the least squares method. Once all the heat flux harmonics have been calculated, the local and instantaneous heat flux through the wall are found using the Fourier series below:

$$\varphi_w(x,t_k) = \frac{\widetilde{\varphi}_w(0,t_k)}{L} + \frac{2}{L} \sum_{i=1}^{14} \widetilde{\varphi}_w(i,t_k) cos(\omega_i x) \tag{10}$$

Although Beck's method is very efficient in applications like ours, the number of future time steps n_{fts} used to regularize the inversion must be very carefully chosen. The hypothesis of future heat fluxes being equal to the current one in Beck's method is closer to reality for smaller values of n_{fts}. Consequently, using a high value of n_{fts} may bias the heat flux estimate, which is especially critical when there are fast variations in the heat flux. For this reason, we performed preliminary simulations to choose appropriately the number of time steps used in this study. These calculations were performed using the same conditions, same data acquisition settings and similar heat flux profiles found in our experiments. Appendix A presents this validation process in detail. We found that, for the current problem, using $n_{fts} = 5$ provided optimal heat flux estimates without creating significant bias. Moreover, this validation step also demonstrated that the obtained heat flux profile is only reliable within the region 280 mm $\leq x \leq$ 520 mm, as the accuracy outside this location is poor.

Finally, if we calculate Eq. 8 using the heat flux harmonics estimated by the inverse method and setting $z = 0$, we obtain the harmonics of the surface temperature difference $\widetilde{\theta}_s(0, i, t)$, which allows us to estimate the temperature evolution of the wall surface temperature $T_s(x, t)$ by the following Fourier series:

$$T_s(x, t_k) = T_{w,0} + \frac{\widetilde{\theta}_s(0, 0, t_k)}{L} + \frac{2}{L}\sum_{i=1}^{14} \widetilde{\theta}_s(0, i, t_k) cos(\omega_i x) \tag{11}$$

and the transverse heat flux $\varphi_x(x, t)$ at the surface in the x-direction using Fourier's law:

$$\varphi_x(x, t_k) = -\lambda \left(\frac{\partial T_s}{\partial x}\right)_{z=0} = \frac{2}{L}\sum_{i=1}^{14} \omega_i \widetilde{\theta}_s(0, i, t_k) sin(\omega_i x) \tag{12}$$

Note we are using in this article the subscript s for the surface temperature, which is estimated, and w for the near-wall temperature measured by the thermocouples.

4.2. Position and velocity of the rewetting front and maximum cooling rate (MCR) point

Finding the rewetting front position is complicated in metal cooling experiments, especially in large scale, because data must be obtained using thermocouple measurements or images from distant cameras, which have some limitations. Moreover, there is a complex transition with different heat transfer processes between the film boiling and wet regimes (Fig. 1). In this study, we used data from the thermocouples to identify the rewetting front and the maximum cooling rate (MCR) positions. Based on their definitions presented earlier, the following hypotheses were made to define their positions: 1) the MCR point corresponds to where the temperature derivative with time is maximum in magnitude; 2) the rewetting front enhances the heat transfer between the wall and the impinged jet, so we should observe an increase in the cooling rate. Note this second hypothesis of intensified heat transfer corresponds to what Gunnerson and Yackle [30] call "quenching", which they differ from "rewetting". However, as we defined in the beginning of section 2, we called "wall rewetting" the departure from film boiling where transition boiling takes place, which results in an increase in the heat dissipation by the impinging jet.

Figure 4 presents on the upper part how we obtained these two locations using thermocouple data. Once we had the temperature evolution for each thermocouple after a cooling experience, each temperature curve was transformed into a Fourier series to eliminate measurement noises in the calculation of its temperature derivative. Then, the derivatives peaks found with the thermocouples located between the jet impingement point and the last thermocouple

(TC7 to TC15) provided the instant when the MCR occured. Consequently, we can correlate these times with the thermocouples locations and trace the temporal evolution of the MCR position. Since wall rewetting occurs before the MCR, we can estimate the rewetting front position by sweeping the temperature derivative regressively from the MCR point and finding the instant when the temperature derivative reaches an established threshold, which is always slightly higher in magnitude than the mean derivative value up to this point. For few exceptions, like TC9 in Fig. 4, the derivative can have an inflection because the arrival of the jet to the impingement location can disturb the temperature profile, as we present in the results. In these cases, the rewetting point was set at the inflection point. Because the temperature derivative is practically the same until wall rewetting takes place, a small increase in the local cooling rate means that the heat transfer phenomenon changed, as we stated in our hypothesis. The threshold calculation was established as the mean value of the temperature derivatives before rewetting (for all thermocouples) minus twice the standard deviation of this population. For the example presented in Fig. 4, the threshold was -2.6 °C/s. Therefore, we were able to distinguish the transition phenomenon for each experiment (Table 2) without setting a unique and arbitrary value for all the test cases. Finally, we can trace the temporal evolution of the rewetting front position by correlating the thermocouples positions and the time of local variation in the temperature derivative.

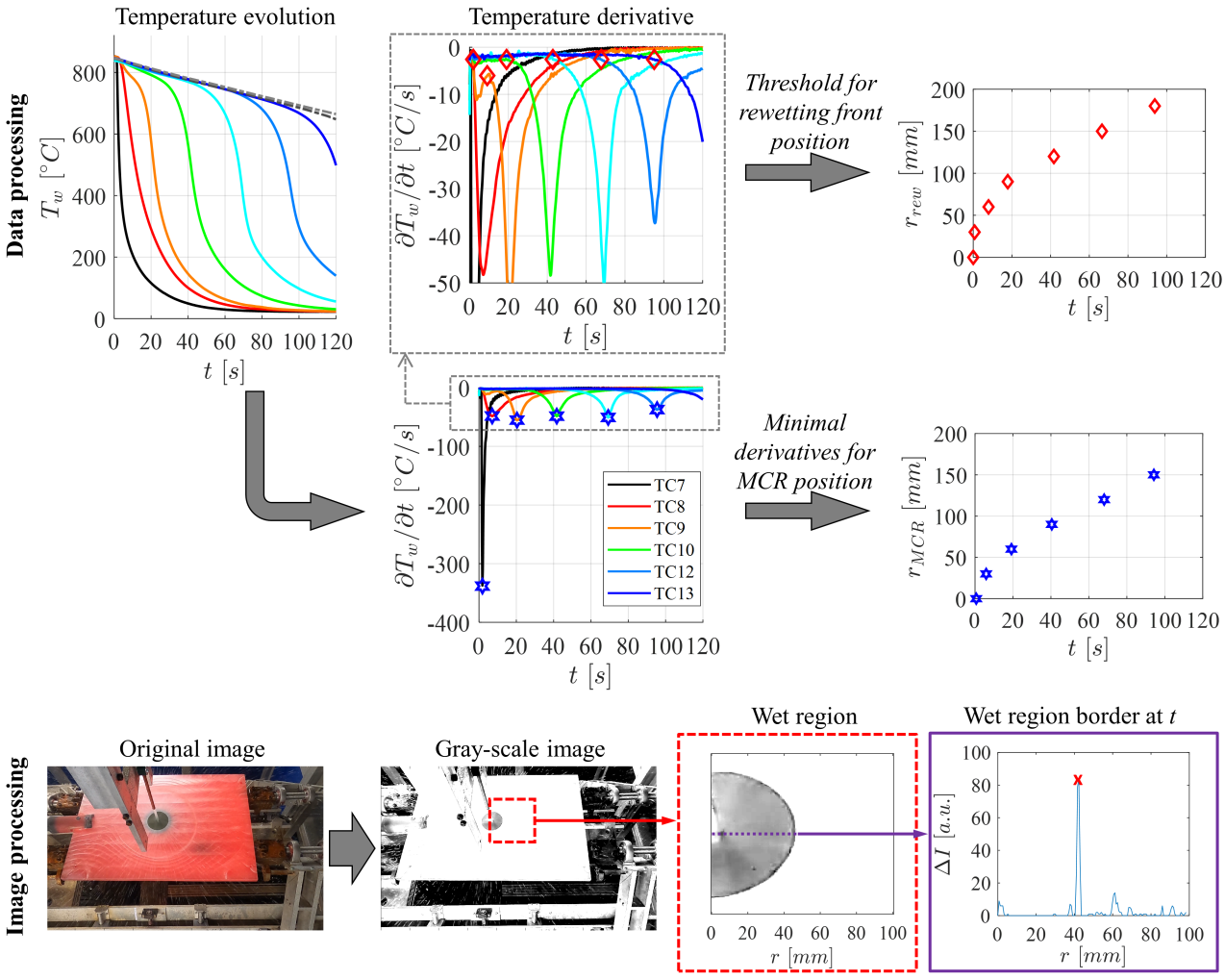

Figure 4: Methods to obtain the MCR point and rewetting front positions with thermocouple data and images.

We validated the method to estimate the MCR position by comparing the results with the wet region evolution obtained by image processing (Fig. 4 in the bottom). In the example presented in Fig. 4, we can easily distinguish the wet region, where single-phase convection and nucleate boiling takes place, as the darker area around the jet impingement point. The border of this region, where the bubble formation is more intense, can be identified changing the image to gray-scale and finding the point where the pixel intensity variation (ΔI) is the highest. The distance between the jet impingement point and the border is estimated by counting the number of pixels between them, and the pixel size was estimated using the plate length as a reference. Figure 5 presents an example with results from test 5 using the thermocouple data processing for the MCR front and image processing methods, and we see a good match between them. The progression of the rewetting front is also presented in the same graph. Moreover, the evolution of the MCR position r_{MCR} and the rewetting front position r_{rew} can be described by a power law with time t as given below:

$$r_{MCR} \text{ or } r_{rew} = At^b \tag{13}$$

We observe a good agreement between the fitted curves and experimental results (Fig. 5). Note that the origin of r_{MCR} and r_{rew} is at the jet impingement point. Hence, we can estimate the MCR and the rewetting fronts velocities with the derivative of this equation, i.e.:

$$v_{MCR} \text{ or } v_{rew} = Abt^{b-1} \tag{14}$$

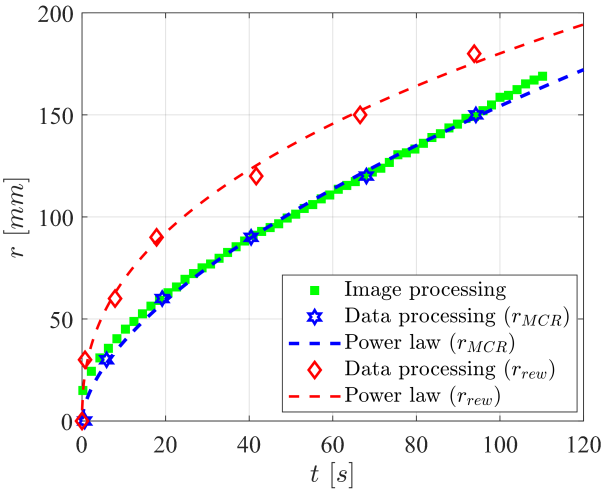

Figure 5: Image processing results for the wet region and data processing results for the MCR and rewetting fronts positions with their corresponding fitted power laws (test 5).

For the results presentation, we used the data processing results for the MCR and rewetting front positions to find the values for the power law coefficients A and b using the least squares method. The image processing results were only used to validate the other method, as presented in this section.

We should highlight that the MCR point does not correspond necessarily to the MHF location. The latter occurs when the temperature derivative in space is maximal, as dictated by Fourier's Law, while the former takes place when the heat flux derivative in space is maximal, according to the heat equation. In fact, the MCR takes place

a little before the MHF, as we demonstrate it in the results section. Therefore, the MCR point is located between the rewetting front and the MHF, which means it is in the rewetting region with transition boiling heat transfer (Fig. 1). We could also find the MHF position using the time when the estimated heat flux is maximal over each thermocouple. However, employing directly the temperature data is advantageous because it allows using all the thermocouple measurements to trace its evolution without being limited to the region where the inverse method is reliable, as discussed in the previous section.

Another important point to discuss is the hypothesis used to identify the rewetting front position, which suggests that only the heat loss to the environment is responsible to decrease the sample temperature before the arrival of the rewetting front. Nevertheless, as we present in the results, the transverse heat flux (φ_x) is not negligible and can increase the local cooling rate. With that information, one could deduce that the threshold actually identifies the onset of transverse heat flux instead of the rewetting front position, which is true as we present in the results. However, the results analysis showed that the dissipated heat flux (φ_w) increases few seconds after the identified rewetting point, which means that the heat dissipation was indeed enhanced as stated in the second hypothesis.

4.3. Parameters uncertainties

In the list below, we present measurement uncertainties:

- Wall temperature: 1 °C;
- Fluid temperature: 2 °C;
- Water flow rate: 0.5 l/min;
- Thermocouple positions: 0.1 mm;

Using the thermocouple position uncertainty and a measured temperature noise of 0.2 °C in a Monte Carlo simulation (like for the heat flux uncertainty in Appendix A), we found the following uncertainties for estimated parameters:

- Heat flux: 0.2 MW/m^2;
- Surface temperature: 2 °C;

The rewetting front position itself has the same uncertainty as the thermocouple positions (0.1 mm) but the time at which the rewetting front passes over the thermocouple position has a higher uncertainty. On the one hand, for thermocouples closer to the jet impingement location, this time uncertainty is much lower and almost independent of the selected threshold ($(\partial T_w/\partial t)_{rew}$). On the other hand, the rewetting front identification with thermocouples more distant from the impact location is more sensitive to the threshold and, hence, its time uncertainty is higher. Testing different threshold values showed that the time uncertainty is negligible for the first three thermocouples (less than 1 s), while it can vary by 5 s for the other thermocouples. Moreover, as mentioned before, there can be a delay between the identified rewetting front position and the increase in the dissipated heat flux because of the effect of transverse heat fluxes, which can affect detecting the true position. This delay is negligible for the first three thermocouples (less than 2 s) and is usually between 2 and 8 s for the other thermocouples. However, the use of linear regression

to find the coefficients in Eq. 13 reduces the error on the measurement of the rewetting front position. The MCR position, in turn, has an almost negligible uncertainty (about 1 mm), as demonstrated in Fig. 5.

5. Results and discussion

The presentation of the results is structured as follows: a complete presentation of the results for one experiment to discuss the involved phenomena; comparison of different test results to evaluate the Reynolds number effect; then another comparison to analyze the jet nozzle diameter effect; and a last comparison of the present results with other experiments in the literature that were performed in a smaller scale (some of those presented in Table 1).

5.1. Results of one jet-cooling experiment (test 5)

We chose to present in detail the results of test 5 (Re_j = 59,000, d_n = 8 mm) before analyzing the Reynolds number and the nozzle diameter effects. Figure 6 presents the cooling curve for each thermocouple inserted in the test sample. The thermocouples numbering increase in the x-axis, reminding that TC1 is at x = 190 mm and TC15 at x = 610 mm, and the jet impingement location is over TC7 at x = 390 mm. For better readability of the results, thermocouples that are symmetric to TC7 have the same color, while TC7 is represented by a black solid line. Also, dashed lines represent thermocouples up to TC6 and solid lines those from TC8. These results show that, as expected, regions closer to the jet impingement point are cooled earlier and faster, with the stagnation point (TC7) being the location cooled most rapidly. For these experimental conditions and experimental duration (120 s), the thermocouples TC14 and TC15, which are too far from the jet, did not present any significant change in the cooling rate, thus that region was only cooled in the film boiling regime. In the same figure, we present as well the rewetting and MCR points with a diamond and a star symbol, respectively. The results show that the adopted method to find these points was apparently very efficient to identify where the trend in the cooling curve changes (for the rewetting point) and where the cooling rate is maximal. Notice that we only presented these points for thermocouples TC7 to TC12. This is because the jet nozzle sweeps over thermocouples TC1 to TC6 before the cooling experiment to reach its impact position, causing a momentary wall rewetting over them (Fig. 7). Even though this course lasts only about 1 s, it is enough to reduce the local temperature by 20 to 50 °C, as we can see in the zoom at the bottom of Fig. 6. For this reason, we only used the data from TC7 to TC15 to obtain the rewetting and MCR positions with the data processing explained in section 4.2.

A brief discussion about the rewetting and MCR temperatures is necessary because their values are much higher than the thermodynamic limit of liquid superheat, also called spinodal temperature (about 320°C at ambient pressure), or even of the water critical temperature (about 374°C, with the critical pressure being approximately 221 bar). These high rewetting and MCR temperatures, between 400°C and 850°C, were observed for all the tested conditions shown in Table 2, which means the solid-liquid interface would be between 365°C and 773°C (according to the solution of two semi-infinite body being in perfect contact [31, 32]). However, this should be physically impossible as water cannot exist in the liquid state above the spinodal temperature, which means solid-liquid contact is impossible at this interface temperature, as attested by recent experimental studies using optical techniques with jet impingement [33] and droplet impact onto hot surfaces [32, 34]. Ohtake and Koizumi [35] also reported in 2004 with

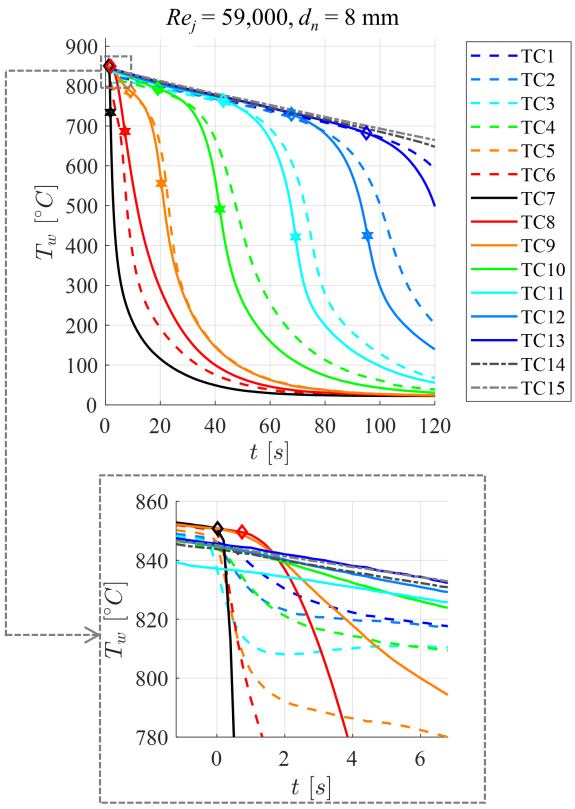

Figure 6: Cooling curves for test 5, with evidence in the first 8 s in the bottom figure. Diamond (⋄) and star (✡) symbols represent, respectively, the instant when the rewetting and MCR fronts pass over each thermocouple.

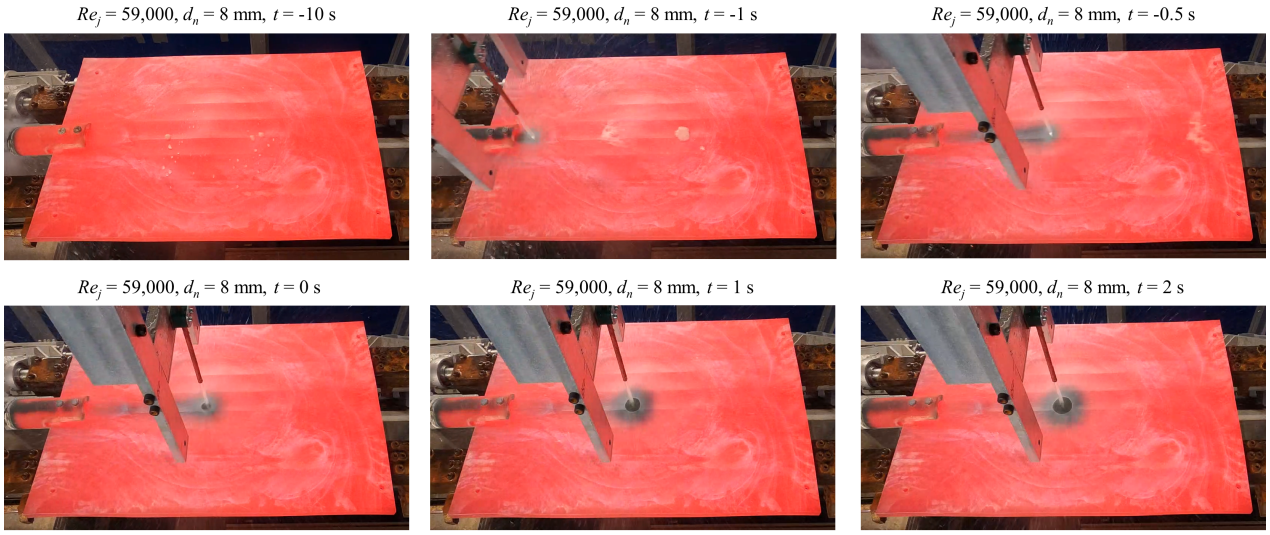

Figure 7: Pictures of moments before and after starting the cooling experiment, showing the jet sweeping over the thermocouples in the left half of the test sample.

film boiling experiments using a thin platinum wire that the vapor film cannot collapse while the interface temperature exceeds a maximum value related to the thermodynamic limit. Despite this contraction, we still find several studies reporting rewetting temperatures substantially higher than the spinodal temperature, as those presented in Table 1. The reason why such high rewetting temperatures are still reported, as in the present study, is the use of

thermocouples for instrumentation, which are accessible temperature sensors but have two important limitations.

First, in ideal conditions (no response time nor thermal contact resistances), thermocouples measure a local mean temperature of the points with which its hot junction is in contact. Therefore, in the case there is a local temperature decrease at the surface to below the spinodal temperature, allowing the establishment of a solid-liquid contact, the thermocouple may not be able to capture this phenomenon because, at its position, the temperature may still be substantially higher. In other words, points at the surface may be at a much lower temperature than the thermocouple instrumentation can capture because of a delay in heat diffusion. This has been very well described and analyzed by Yagov et al. [31] with a critical review of past experiments and numerical simulations. They demonstrated that, within 0.1 s, fast temperature transients can take place with an intense heat dissipation at the crests of surface microprotrusions such that the local surface temperature is substantially lower than the measured by an idealized thermocouple (again, no response time nor thermal contact resistances) located 0.2 mm from the protrusions base. This is in accordance with the experimental observations by Gomez et al. [33], who explains the possibility of having wall rewetting at wall temperatures higher than the spinodal because of a cyclic explosive bubble formation regime at surface peaks that occurs at very high frequencies (up to 40 kHz), where we could have locally an intense heat exchange. Castanet et al. [32] showed using infrared thermography that the surface temperature can decrease by 140°C (initially at 550°C) during a single water droplet impact in less than 12 ms, which certainly would not be measured equally by a thermocouple located close to the heat exchanging wall. These studies, as well as the one by Ohtake and Koizumi [35], explain why it is common to find rewetting temperatures higher than the spinodal in fast temperature transients. Yagov et al. [31] even discuss the establishment of the solid-liquid contact with more details: if the heat sink promoted by an instantaneous solid-wall contact at the protrusion crest is higher than the heat diffusion from the solid body to the crest, this rewet area will still exist or even expand; otherwise, the heat diffusion will reheat the crest and film boiling is restored.

Second, thermocouples measure actually their own temperature (at the hot junction), not the sample temperature. Therefore, because they have their own thermal inertia and thermal contact resistances exist when attaching the sensor to the sample, there is a response time in the measured temperature response that filters high frequency processes. In transient measurements, the measured temperature $T_{w,mes}$ at a time step k caused by a response time τ can be simulated by [38]:

$$T_{w,mes}(t_k) = T_{w,real}(t_k) + \left[T_{w,mes}(t_{k-1}) - T_{w,real}(t_k)\right] e^{(-\Delta t/\tau)} \tag{15}$$

which means the difference between measured and surface temperatures might be even larger than the evaluated by Yagov et al. [31] because of the delay in the thermocouple response to measure the real local temperature $T_{w,real}$. The thermocouples we used in our experiments have a response time of about 0.3 s, which are appropriate for large scale experiments like ours but cannot capture fast transients like those observed by Castanet et al. [32] or Gomez et al. [33]. We present in section 5.4 comparisons of the present experimental results with some available in the literature and we discuss in more detail the thermocouple response time effect with a simulation of the thermocouple signal using Eq. 15 in a fast transient with a high heat flux obtained by Nobari et al. [17], showing the difference between the real and measured temperatures could be as high as 200°C. Hence, the conjugated effects of lower local temperatures and thermocouple response time may explain why we found rewetting temperatures much higher than

the thermodynamic limit.

These thermocouple measurements (Fig. 6) were used in the inverse method explained in section 4.1 to estimate the dissipated heat flux φ_w, whose temporal evolution is presented in Fig. 8a. We can correlate the heat flux with the estimated surface temperature to plot the boiling curve for each thermocouple, as shown in Fig. 8b. In these figures, only the thermocouples in the reliable region, between 280 mm (TC4) and 520 mm (TC12), are presented. The highest heat flux is found with TC7 at the stagnation point and it decreases as the thermocouple location is more distant from the jet impact. This has already been observed by several authors in the past [12, 17, 20, 22, 23] The rewetting and MCR points are again displayed. The rewetting point occurred few seconds before the heat flux increased for all the thermocouples, respecting our hypothesis to identify this point. Also, it occurred almost instantaneously for TC7, at the stagnation zone, and its neighbors (TC6 and TC8), which impeded the observation of the film boiling regime over these thermocouples. For the other thermocouples, we could observe a short heat flux plateau, characteristic of film boiling, before wall rewetting took place. As discussed in section 4.2, the MCR point identified with the cooling curve occurred a few seconds before the MHF found by the inverse method (Fig. 8a). Finally, the heat flux found over the TC10 was higher than over TC4, while the heat flux over TC6 was higher than over TC8, their respective symmetrical thermocouples with the jet impingement point. This might be an effect of the jet sweeping the first thermocouples before the cooling experiments. For this reason, we only present boiling curves with thermocouples TC7 to TC12 when analyzing the jet Reynolds number and nozzle diameter effects.

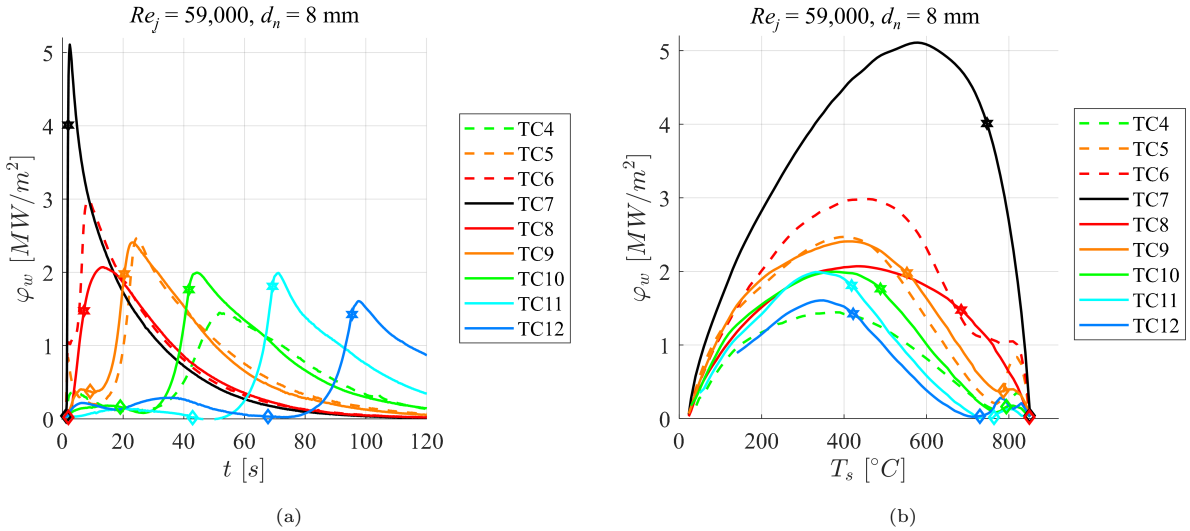

Figure 8: Time evolution of the dissipated heat flux (a) and boiling curves (b) for each thermocouple of test 5. Diamond (⋄) and star (✡) symbols represent, respectively, the rewetting and MCR points.

We can also evaluate the dissipated heat flux profiles along the x-direction at different moments after the cooling experiment have started (Fig. 9). In the first seconds, we observe a high peak at the jet impingement point over TC7 at 370 mm. This peak decreases as the heat flux increases progressively over neighboring thermoucouples. At 30 seconds after starting the cooling test, two peaks in opposite directions appear and, as the jet cooling continues, they become more distant and the MHF decreases. By the end of the experiments, at 90 s, the heat flux in the middle is already negligible because this region was already cooled but the MHF is still taking place near TC11 at 490 mm. We remark that the simulated heat flux in Appendix A to validate our inverse method is very similar to

the experimental profile, which increases the reliability of the estimated heat flux.

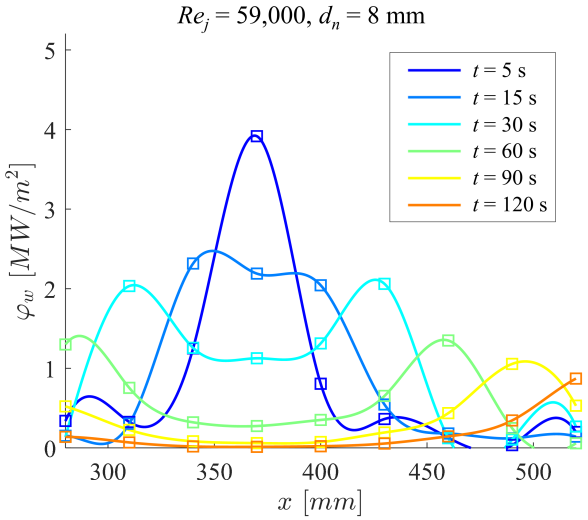

Figure 9: Reconstructed heat flux profile in the reliable region with test 5 at different times after starting the cooling experiment.

In Fig. 10, we present the estimated transverse heat flux (Eq. 12) at the location of each thermocouple with test 5. At the stagnation point, over TC7, the transverse heat flux is negligible throughout the cooling test. For the other thermocouples, the transverse heat flux is also almost zero before wall rewetting but it increases rapidly during wall rewetting and decreases very slowly with the decrease in the surface temperature, reaching zero again when the wall surface has been completely cooled. This happens because the transition from film boiling regime to transition boiling and nucleate boiling creates a temperature gradient in the x-direction and, hence, generates this transverse heat flux. For this reason $\varphi_x > 0$ for TC4 to TC6 while $\varphi_x < 0$ for TC8 to TC12, showing the transverse heat flux is always towards the jet impingement location. An interesting result is that the magnitude of the transverse heat flux is very similar for all the thermocouples and it is not negligible, as it corresponds to more than 20% of the MHF at the stagnation point.

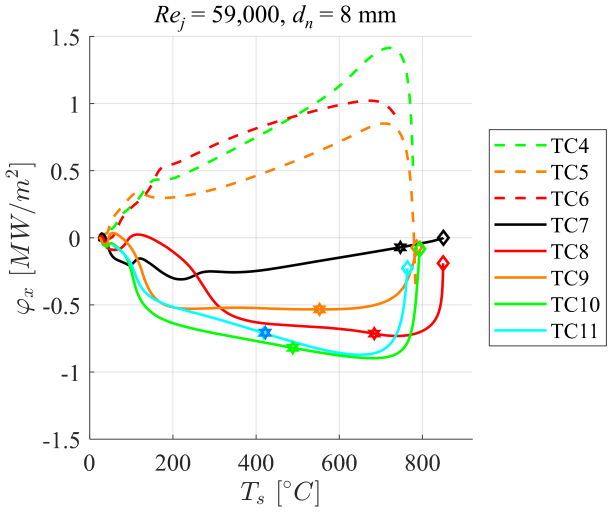

Figure 10: Transverse heat fluxes at the surface for test 5. Diamond (⋄) and star (✡) symbols represent, respectively, the rewetting and MCR points.

Finally we present the rewetting and MCR front positions and velocities in Figs. 11a and b, respectively. As dictated by the sequence of events in the transition from film boiling to single-phase regimes, the wall rewetting occurs earlier than the MCR (reminding that MHF occurs few seconds later than MCR). The depart from film boiling regime due to wall rewetting occurs very fast for the region neighboring the stagnation point but after the rewetting front velocity decreases rapidly. As shown in Fig. 11b, its velocity starts at around 100 mm/s and ends slightly lower than 1 mm/s, which is coherent with the fact that the fluid velocity decreases in the radial direction from the stagnation point [17]. The MCR front behavior is similar to the rewetting front but its initial velocity is much lower, about 30 mm/s. However, at the end of the experiment, both the MCR and rewetting fronts have approximately the same velocity. For this test, the power law coefficients (Eq. 13) were $A_{rew} = 26.6$ and $b_{rew} = 0.416$ for the rewetting position and $A_{MCR} = 9.80$ and $b_{MCR} = 0.599$ for the MCR position, calculating the positions in mm and the velocities in mm/s (with Eq. 14). It is worthy mentioning that, even though there is a relatively large delay between the detected rewetting front arrival time and the onset of the dissipated heat flux, about 8 s for TC10 to TC12 as shown in Fig. 8a, the delays between the rewetting and MCR fronts arrival times are much larger for the same thermocouples, between 20 s and 30 s. This means that wall rewetting occurs significantly earlier than the MCR and, consequently, before the arrival of the dark zone area seen in the image processing (Fig. 4).

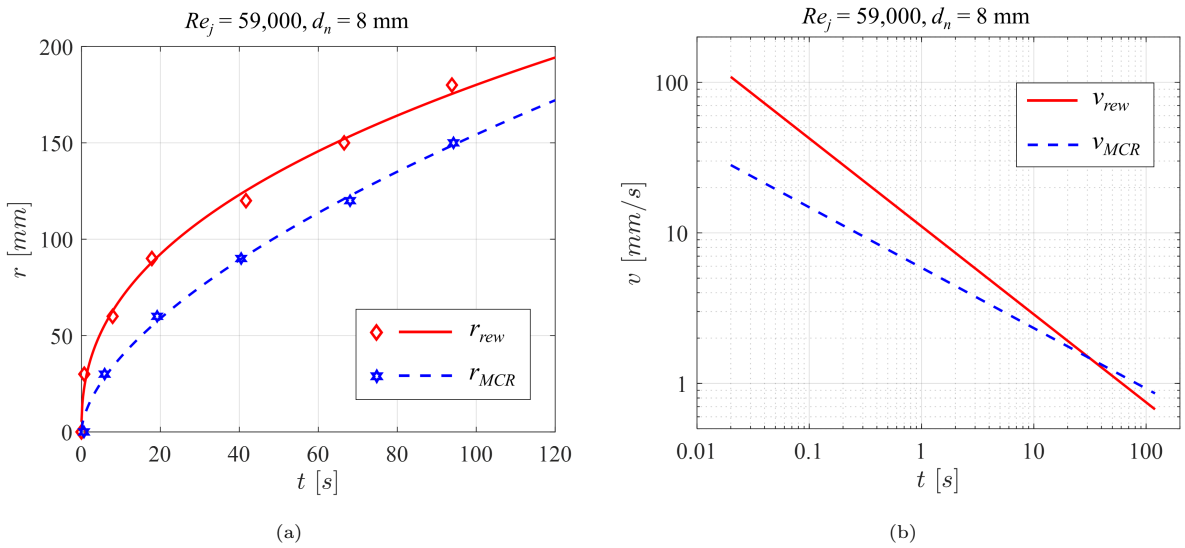

Figure 11: Rewetting characteristics for test 5: a) rewetting and MCR positions, where symbols are the points identified by data processing and lines are fitted power laws; b) rewetting and MCR fronts velocities estimated with the identified power law coefficients.

5.2. Effect of the jet Reynolds number

Having presented the experimental results in detail for one test, we can now analyze the parametric effects tested in this study, starting with the jet Reynolds number for a fixed nozzle diameter of 10 mm. Figure 12 presents boiling curves of the dissipated heat flux for different Reynolds numbers and different thermocouples (TC7 at the impact point and TC9 and TC11 that are 60 and 120 mm from TC7). Lines with the same color correspond to the same test condition, while lines of the same type are for the same thermocouple. We present again the rewetting and MCR points with diamond and star symbols. At the jet impingement point (TC7, solid lines), the increase in the Reynolds number resulted in the increase in the MHF. Nevertheless, this increase was more substantial from Re_j = 9,800 to

Re_j = 23,500 (about 18%) and varied less than 10% from Re_j = 23,500 until Re_j = 120,000. For thermocouples farther from the impingement location, the Reynolds number effect becomes more significant on the dissipated heat flux. For TC9 (dashed lines), for example, φ_w = 4.0 MW/m^2 with Re_j = 120,000 whereas it is only 1.1 MW/m^2 for Re_j = 9,800, while φ_w = 3.0 MW/m^2 for TC 11 with Re_j = 120,000 whereas it is not even observed with Re_j = 9,800 during the 120 s of experiment.

The results for the transverse heat flux for all the jet Reynolds numbers (Fig. 13) are practically the same as those obtained with test 5. Transverse heat exchange is virtually zero at the stagnation point, while, for other locations, its magnitude increases when the rewetting front arrives (as demonstrated by the diamond symbols in the graph) and then decreases. Not only the transverse heat flux was very similar for all the thermocouple positions, as we saw in Fig. 10, it was also insensitive to the jet Reynolds number in the framework of our tests. This demonstrates that the temperature gradient in the x-direction that promotes the transverse heat flux is fully established much faster than the progress of the rewetting front over the plate surface. In other words, if the temperature decrease after the wall rewetting was slower than the rewetting front velocity, the temperature gradient would be dependent on the rewetting front velocity, but it was not the case in the present experiment as demonstrated in Fig. 13.

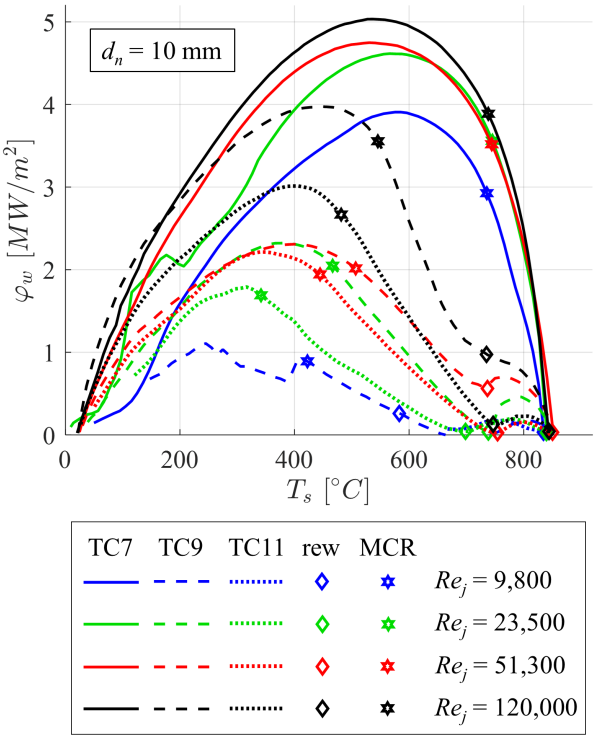

Figure 12: Boiling curves for different jet Reynolds numbers with d_n = 10 mm. Diamond (◇) and star (✡) symbols represent, respectively, the rewetting and MCR points.

Concerning the wall rewetting characteristics, Figure 14 presents the expected result: both the rewetting and the MCR fronts advances faster with the increase in the Reynolds number. As observed in the previous section with test 5 results, the rewetting front velocity is higher than the MCR front velocity in the beginning of the experiment, but they tend to have the same velocity once the wet region becomes larger. The power law coefficients found for each test (including those for test 5 with a different nozzle diameter) are given in Table 3. The power law coefficients for

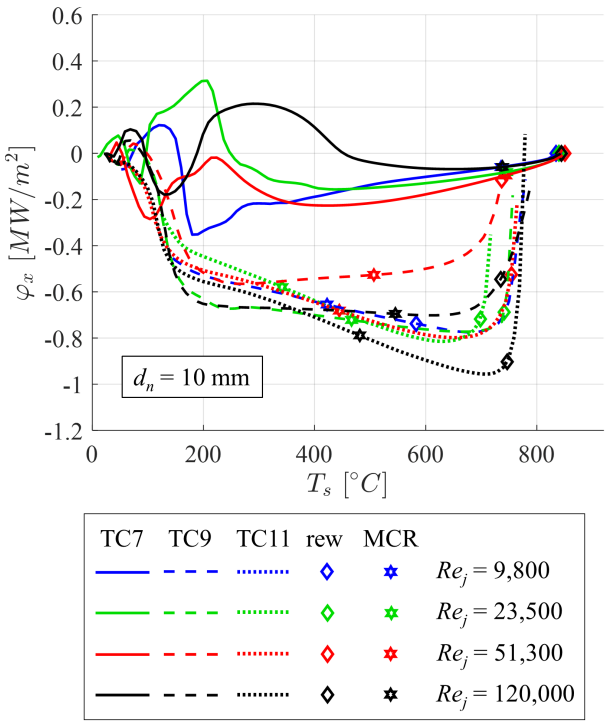

Figure 13: Transverse heat fluxes at the surface for different jet Reynolds numbers with $d_n = 10$ mm. Diamond (◇) and star (✡) symbols represent, respectively, the rewetting and MCR points.

the MCR (b_{MCR}) is not very close to 0.5, which was reported by Hatta et al. [39] for a "black zone area" during the cooling using a similar image processing method as ours. Nevertheless, the coefficient for the rewetting front position (b_{rew}) is approximately 0.5, even though this front does not correspond to the dark area in the images, as we presented in section 4.2.

Table 3: Obtained power law coefficients for each experiment for the rewetting and MCR fronts position (Eq. 13, in mm) and velocity (Eq. 14, in mm/s).

Test	d_n	Re_j	A_{MCR}	b_{MCR}	A_{rew}	b_{rew}
1	10	9,800	1.32	0.877	8.25	0.473
2	10	23,500	5.01	0.704	9.82	0.589
3	10	51,300	9.79	0.609	22.8	0.448
4	10	120,000	17.0	0.565	30.0	0.450
5	8	59,000	9.80	0.599	26.6	0.416

5.3. Results with different nozzle diameters

We compare herein the results from test 3 ($Re_j = 51{,}300$ and $d_n = 10$ mm) and 5 ($Re_j = 59{,}000$ and $d_n = 8$ mm), which means similar Reynolds numbers (approximately 55,000) but different nozzle diameters. Although both tests were performed with a water flow rate of 20 l/min, reducing the nozzle diameter leads to a jet velocity 51% higher for

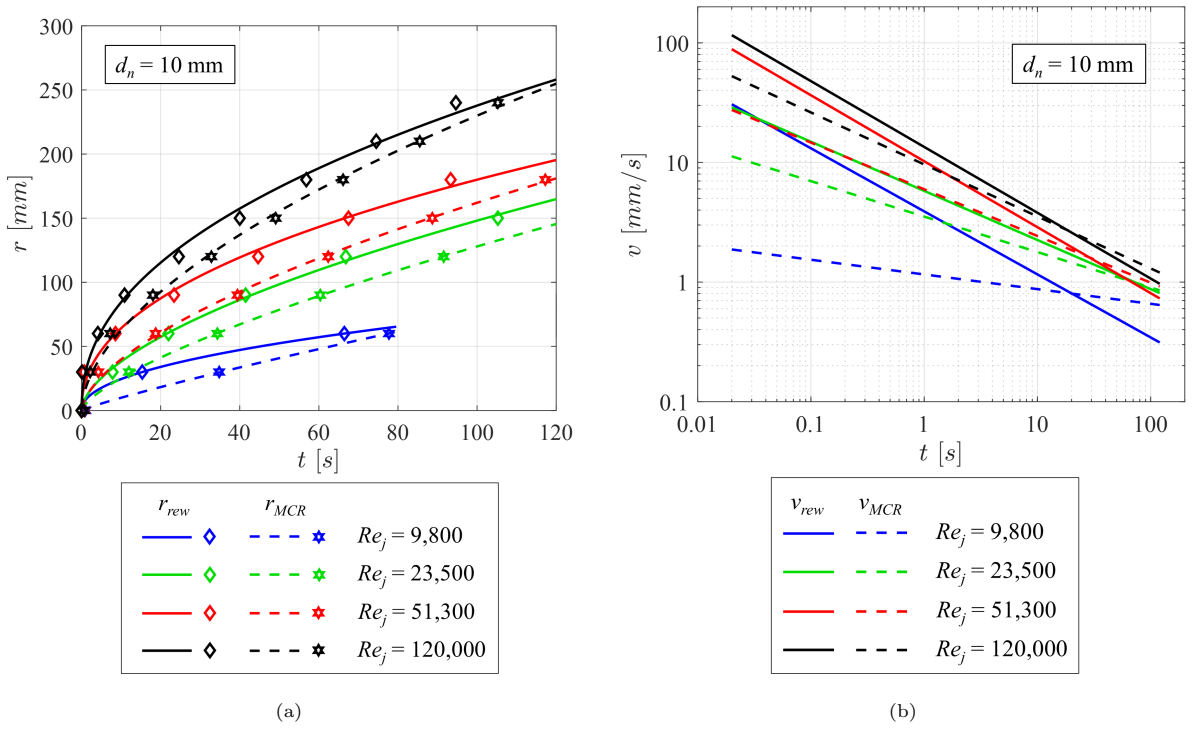

(a) (b)

Figure 14: Rewetting characteristics for different jet Reynolds numbers with d_n = 10 mm: a) rewetting and MCR positions, where symbols are the points identified by data processing and lines are fitted power laws; b) rewetting and MCR fronts velocities estimated with the identified coefficients for the power law.

test 5 than test 3 (v_j = 6.8 and 4.5 m/s, respectively). This small difference in the test configuration did not result in significant changes in the boiling curves for the dissipated heat flux (Fig. 15), especially over thermocouples TC9 and TC11, which are more distant from the impact location. At the stagnation zone, i.e. over TC7, the MHF is slightly higher with the smaller nozzle diameter, which may be an effect of the higher jet velocity that enhanced locally the heat dissipation. The rewetting and MCR temperatures were as well very similar for both configurations, as well as the transverse heat flux behavior (Fig. 10 and 13). Likewise, no substantial difference was observed between the evolution of the rewetting and MCR fronts for test 3 and 5 (Fig. 16), which means that their velocities were also the same for both tests. These results suggest that the stagnation zone may be affected by the jet velocity, as an increase in this parameter resulted in a slight increase in the heat dissipation by the impinging jet. However, out of the stagnation zone, the heat transfer and the rewetting hydrodynamics process are almost identical in a macroscale observation because the water flow rate is the same for both cases and the variation in the jet diameter becomes negligible compared to the test scale.

5.4. Comparison with previous studies

In this section, we compare the present results with similar ones found in some of the studies listed in Table 1 [17, 18, 20, 24]. The large variety of experiments in the literature makes it difficult to compare different experimental results, because there are some differences either in the experimental conditions, like initial sample temperature or water flow rate, or in the configuration, like the jet diameter or sample size. Instrumentation problems can also exist and are rarely reported in scientific papers although they affect the results, like the presence of metal

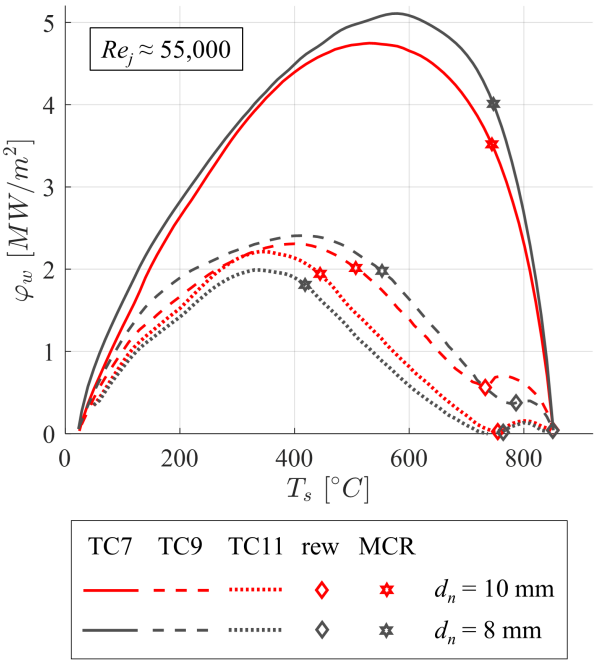

Figure 15: Boiling curves for different nozzle diameters with $Re_j \approx 55{,}000$. Diamond ($\diamond$) and star ($\star$) symbols represent, respectively, the rewetting and MCR points.

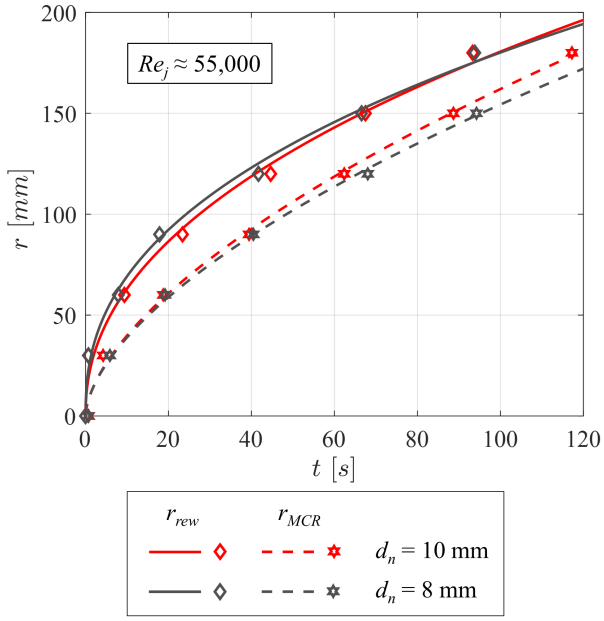

Figure 16: Rewetting and MCR front positions for different nozzle diameters with $Re_j \approx 55{,}000$, where symbols are the points identified by data processing and lines are fitted power laws.

swarf that increases the sample-thermocouple thermal contact resistance and disturbs the thermocouple positioning. Furthermore, the tested materials are also different and oxidize differently. While the oxide layer with nickel (our material) and 300-series stainless steels (used by Karwa and Stephan [20] and Wang et al. [24]) is stable, materials like the HSLA (used by Nobari et al. [17]) form scales, which affects the cooling process [36]. Nevertheless, this careful comparison is helpful to understand how the present experiments performed at a larger scale are situated

among those performed at a laboratory scale.

Figure 17 presents boiling curves for the dissipated heat flux by the jet of test 2 (Re_j = 23,500 and T_j = 25 °C) for TC7, at the impact location, and TC8, 30 mm away from TC7. We compare these results with the ones obtained by Nobari et al. [17] with Re_j = 36,300 and T_j = 25 °C and with results by Wang et al. [24] with Re_j = 18,000 and T_j = 23 °C, both for a thermocouple at the stagnation point and one being 40 mm distant from the jet impact location. The heat fluxes obtained by Nobari et al. are almost three times higher than those reported herein and by Wang et al, who found very similar heat fluxes despite the difference in the initial samples temperature (850 °C in this study, 650 °C in theirs). To the authors' opinion, the most probable cause for these higher values found by Nobari et al. is the faster response time of their thermocouples. They used thermocouples with exposed wires (0.25 mm diameter) that were spot-welded directly to the sample, which ensures much faster temperature response, although it is a very fragile instrumentation. Karwa and Stephan [20], for instance, used grounded sheathed thermocouples with 0.5 mm diameter that were inserted into holes with thermal paste and found MHF higher than 9 MW/m^2 at the stagnation zone with Re_j = 18,000 and T_j = 25 °C. In turn, we used ungrounded sheathed thermocouples with 1 mm diameter inserted into holes without thermal paste while Wang et al. used thermocouples with 3 mm diameter inserted with thermal paste, which are more robust to withstand the experimental conditions but they have a lower response time that reduces the temperature temporal resolution, which may explain both lower heat fluxes results. Although not listed in Table 1, Gradeck et al. [40] found a MHF of about 12.5 MW/m^2 with Re_j = 12,500 and T_j = 20 °C using back-face infrared thermography (IRT) in a 5-mm thick nickel disk and an inverse method based on Hankel transform. Even though their temperature measurement was relatively far from the heat-exchanging surface (5 mm), they still found high MHF values, showing how important the temperature measurement response is, as IRT measurements are virtually instantaneous. Agrawal et al. [18] found a MHF of about 1.8 MW/m^2 at the stagnation zone with Re_j = 24,000 and T_j = 22 °C using thermocouples with wire diameter of 0.25 mm to measure the sample temperature. However, their sample was a thin stainless steel plate with 0.25 mm thickness, which has a much lower thermal inertia than the samples used in this study and by the other authors.

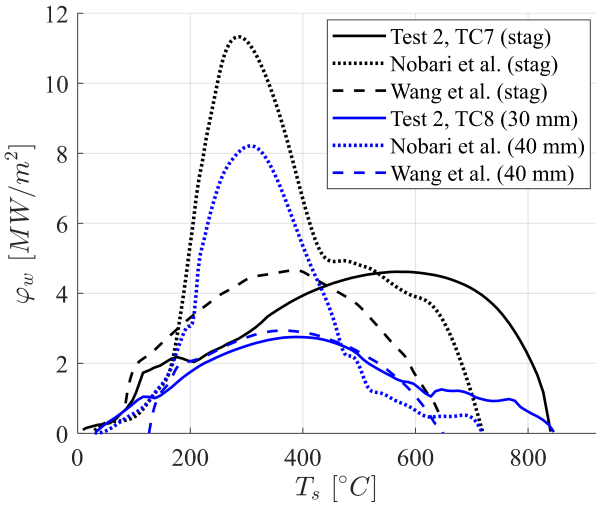

Figure 17: Boiling curves of test 2 (Re_j = 23,500 and T_j = 25 °C) for TC7 (in the stagnation zone) and TC8 (30 mm from the stagnation zone) compared with results in the literature: Nobari et al. [17] (Re_j = 36,300 and T_j = 25 °C) and Wang et al. [24] (Re_j = 18,000 and T_j = 23 °C).

The effect of the thermocouple response time is more evident in Fig. 18a, where we present simulation results of the thermocouple measurement over time at the impact location (no transverse heat flux, hence a 1D problem) applying at the boundary a heat flux evolution obtained by Nobari et al. [17] shown as a solid black line in Fig. 18b. This heat flux evolution corresponds to a different test condition than the one presented in Fig. 17; however, it was measured at the impact location and illustrates well the fast transients they observed in their experimental campaign. The simulated temperature measurements are given as temperature differences $\theta = T - T_0$. Calculations were performed considering a thermocouple with no response time ($\tau = 0$ s), which means the simulated measurement is simply the solution of Eq. 8 for a thermocouple located 0.5 mm from the heat exchanging surface, and considering different response times whose signals can be simulated using the results for $\tau = 0$ s and applying Eq. 15. The chosen response times correspond to estimates for the instrumentation methods used by Nobari et al. [17] ($\tau = 0.02$ s), Karwa and Stephan [20] ($\tau = 0.1$ s), and in this study ($\tau = 0.3$ s), based on datasheet values for water immersion tests. We could not estimate a response time for Wang et al. [24] instrumentation because they did not mention if their thermocouples were grounded or not, which affects substantially the response time for a 3 mm diameter thermocouple. If grounded, the response time should be approximately 0.3 s, similar to our 1 mm ungrounded thermocouple.

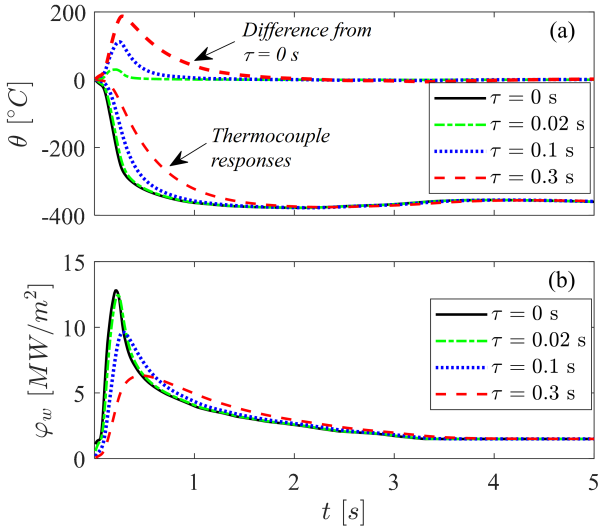

Figure 18: Simulation results presenting the effect of the thermocouple response time on the temperature measurement (a) and the estimated heat flux using (b).

Figure 18a clearly shows that the increase in the thermocouple response time causes a delay in the measurements, as expected, resulting in a difference of up to 200°C from the true temperature ($\tau = 0$ s). As mentioned earlier, this helps to explain why we observed very high rewetting temperatures in the present study. Furthermore, we took the simulated thermocouple signals and used them in our inverse method to estimate the dissipated heat flux. The results are presented in Fig. 18b, showing that the delayed thermocouple responses are interpreted by the inverse method as lower heat flux values that last longer. This confirms that the same experiment would provide very different heat flux estimates depending on the adopted instrumentation method. We should also note that, even though the MHF is estimated very differently for each response time, the integral of the heat flux evolution over time is the same for all the curves (varies by less than 1%), which means the energy balance is always respected independently of the

delay in the temperature measurements.

Finally, Fig. 19 shows the rewetting front velocity as a function of its position from the impact location for test 2 compared with results by Agrawal et al. [18] with Re_j = 24,000 and T_j = 22 °C and Karwa and Stephan [20] with Re_j = 18,000 and T_j = 25 °C. Agrawal et al. found a different profile and much higher rewetting front velocities farther from the impact location than us and Karwa and Stephan, which is probably because of their very thin test sample that facilitates the rewetting front progression due to the wall low thermal inertia. As we observed with the results for test 2, Karwa and Stephan also found a higher rewetting front velocity near the jet impingement location and its progressive decrease with the increase in the distance from the stagnation zone. Nevertheless, the quantitative results are very different for the region near the jet, only having a similar order of magnitude for $r_{rew} > 8$ mm.

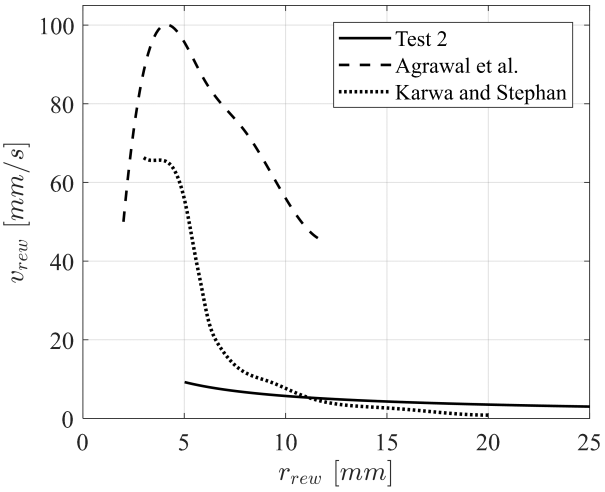

Figure 19: Rewetting front velocity as a function of its distance from the impingement location of test 2 (Re_j = 23,500 and T_j = 25 °C) compared with results in the literature: Agrawal et al. [18] (Re_j = 24,000 and T_j = 22 °C) and Karwa and Stephan [20] (Re_j = 18,000 and T_j = 25 °C).

These comparisons show that the scale of the experiment can play a very important role on the results. The cooling of a plate, a sheet or a cylinder can behave very differently from each other. On the one hand, laboratory scale experiments provide detailed information near the impact location by using more sensitive instruments and sensors. On the other hand, large scale experiments are more representative of industrial applications and allow performing the experiments for longer time and collecting more macroscale data, like the heat dissipation and the progression of the rewetting front relatively far from the impact location.

6. Conclusions

This paper presented experimental results of jet impingement cooling using a large plate, compared to those used in experiments found in the literature, in experimental conditions similar to industrial application. The tested sample was a nickel plate with dimensions of 800 x 500 x 20 mm^3, which was initially at about 850°C and then cooled by a single water jet impacting over its upper surface. Moreover, the plate was instrumented with fifteen thermocouples, whose temperature measurements were used to solve an inverse heat conduction problem to estimate the heat flux over the heat-exchanging surface. Also, the rewetting front position and velocity was estimated using the temperature

data with a method that was validated with results using image processing. In this study, we presented in detail the results for one experiment and evaluated the effect of the jet Reynolds number and nozzle diameter.

The detailed results of test 5 showed that the method to identify wall rewetting over a thermocouple using a calculated threshold for the temperature derivative was very efficient to capture the beginning of fast temperature decrease in the cooling curves. As observed by other researchers, the maximum cooling rate point, where the temperature derivative is maximal, occurred a little earlier than the maximum heat flux. The heat flux was the highest at the stagnation point and it decreased with the increase in the distance from the impact location. Wall rewetting took place very rapidly at the stagnation zone and for neighboring regions, impeding to characterize the film boiling regime at these locations. After tracing the heat flux profile for each time, we observed in the beginning of the cooling a peak heat flux in the stagnation zone and the formation of two peaks that moved in opposite directions in the course of the experiment. The evolution of the rewetting front and the maximum cooling rate positions followed a power law equation with time for all the tests, which allowed estimating as well their velocity for each experiment.

The increase in the jet Reynolds number increased more substantially the dissipated heat flux away from the impact location than in the stagnation zone. Moreover, the decrease in the Reynolds number decreased the velocity of the rewetting front, hence more distant points of the heated surface were not rewet during the 120 s of cooling. Concerning the transverse heat flux (in the x-direction), it was negligible at the stagnation zone for all the tested conditions, as expected. However, out of the stagnation zone, the transverse heat flux increased rapidly when the wall rewetting began and decreased very slowly with the decrease in the wall temperature until the wall rewetting was completed, and its magnitude was independent of the thermocouple position and the jet Reynolds number. Tests with the same conditions but with two nozzle diameters gave practically the same results of the dissipated and transverse heat fluxes and for the rewetting and MCR front characteristics, although the heat flux in the stagnation zone was slightly higher for the smaller nozzle diameter, possibly because the jet impacted at a higher velocity.

Finally, we compared the present results for the dissipated heat flux and the rewetting front velocity with some found in the literature in similar conditions but at a smaller scale. Experiments at laboratory scale can use finer instruments and sensors that allow getting more detailed information, especially in and near the stagnation zone. However, large scale experiments are not only more representative of industrial applications but are also capable to provide more macroscale data.

7. Funding

This work was performed in the frame of the research projects TREMPLIN and RESEM 2020, both managed by the Institut de Recherche Technologique Matériaux Métallurgie Procédés (IRT M2P) and financially supported by the French program Plan d'Investissement d'Avenir (PIA). TREMPLIN is a collaborative project between IRT M2P and the industrial partners ArcelorMittal Global R&D, Ascometal and Vallourec.

References

[1] A. K. Mozumder, M. Ahmed, Jet quenching phenomena during emergency cooling of high temperature solid surface, Energy Procedia 160 (2019) 356 – 363, 2nd International Conference on Energy and Power, ICEP2018, 13–15 December 2018, Sydney, Australia. doi:https://doi.org/10.1016/j.egypro.2019.02.168.

[2] S. Sahu, P. Das, S. Bhattacharyya, An experimental investigation on the quenching of a hot vertical heater by water injection at high flow rate, Nuclear Engineering and Design 240 (6) (2010) 1558 – 1568. doi:https://doi.org/10.1016/j.nucengdes.2010.02.028.

[3] G. Chen, M. Jia, S. Zhang, Y. Tang, Z. Wan, Pool boiling enhancement of novel interconnected microchannels with reentrant cavities for high-power electronics cooling, International Journal of Heat and Mass Transfer 156 (2020) 119836. doi:https://doi.org/10.1016/j.ijheatmasstransfer.2020.119836.

[4] B. Li, T. Cader, J. Schwarzkopf, K. Okamoto, B. Ramaprian, Spray angle effect during spray cooling of microelectronics: Experimental measurements and comparison with inverse calculations, Applied Thermal Engineering 26 (16) (2006) 1788 – 1795. doi:https://doi.org/10.1016/j.applthermaleng.2006.01.023.

[5] S. M. Ammar, C. W. Park, Evaporation heat transfer characteristics of falling film in small diameter fabricated tubes of absorption refrigeration system: An experimental investigation, International Journal of Heat and Mass Transfer 165 (2021) 120618. doi:https://doi.org/10.1016/j.ijheatmasstransfer.2020.120618.

[6] S. Mori, N. Maruoka, K. Okuyama, Critical heat flux enhancement by a two-layer structured honeycomb porous plate in a saturated pool boiling of water, International Journal of Heat and Mass Transfer 118 (2018) 429 – 438. doi:https://doi.org/10.1016/j.ijheatmasstransfer.2017.10.100.

[7] M. Modak, S. S. Chougule, S. K. Sahu, An experimental investigation on heat transfer characteristics of hot surface by using cuo–water nanofluids in circular jet impingement cooling, Journal of Heat Transfer 140 (2018) 012401. doi:https://doi.org/10.1115/1.4037396.

[8] G. Liang, I. Mudawar, Review of spray cooling – part 2: High temperature boiling regimes and quenching applications, International Journal of Heat and Mass Transfer 115 (2017) 1206 – 1222. doi:https://doi.org/10.1016/j.ijheatmasstransfer.2017.06.022.

[9] C. Agrawal, R. Kumar, A. Gupta, B. Chatterjee, Effect of nozzle geometry on the rewetting of hot surface during jet impingement cooling, Experimental Heat Transfer 27 (3) (2014) 256–275. doi:https://doi.org/10.1080/08916152.2013.782375.

[10] A. K. Nallathambi, E. Specht, Estimation of heat flux in array of jets quenching using experimental and inverse finite element method, Journal of Materials Processing Technology 209 (12) (2009) 5325 – 5332. doi:https://doi.org/10.1016/j.jmatprotec.2009.04.001.

[11] M. Gradeck, A. Ouattara, D. Maillet, P. Gardin, M. Lebouché, Heat transfer associated to a hot surface quenched by a jet of oil-in-water emulsion, Experimental Thermal and Fluid Science 35 (5) (2011) 841 – 847, 7th ECI-International Conference on Boiling Heat Transfer – ICBHT-2009. doi:https://doi.org/10.1016/j.expthermflusci.2010.07.002.

[12] C. Gomez, C. van der Geld, J. Kuerten, M. Bsibsi, B. van Esch, Film boiling in quench cooling with high-temperature jets, International Journal of Heat and Mass Transfer 164 (2021) 120578. doi:https://doi.org/10.1016/j.ijheatmasstransfer.2020.120578.

[13] J. Hammad, Y. Mitsutake, M. Monde, Movement of maximum heat flux and wetting front during quenching of hot cylindrical block, International Journal of Thermal Sciences 43 (8) (2004) 743 – 752, selected articles from the ICHMT Symposium 'Transient Convection'. doi:https://doi.org/10.1016/j.ijthermalsci.2004.02.014.

[14] S. G. Lee, M. Kaviany, C.-J. Kim, J. Lee, Quasi-steady front in quench subcooled-jet impingement boiling: Experiment and analysis, International Journal of Heat and Mass Transfer 113 (2017) 622 – 634. doi:https://doi.org/10.1016/j.ijheatmasstransfer.2017.05.081.

[15] S. G. Lee, M. Kaviany, J. Lee, Quench subcooled-jet impingement boiling: Two interacting-jet enhancement, International Journal of Heat and Mass Transfer 126 (2018) 1302 – 1314. doi:https://doi.org/10.1016/j.ijheatmasstransfer.2018.05.113.

[16] H. Wang, W. Yu, Q. Cai, Experimental study of heat transfer coefficient on hot steel plate during water jet impingement cooling, Journal of Materials Processing Technology 212 (9) (2012) 1825 – 1831. doi:https://doi.org/10.1016/j.jmatprotec.2012.04.008.

[17] A. H. Nobari, V. Prodanovic, M. Militzer, Heat transfer of a stationary steel plate during water jet impingement cooling, International Journal of Heat and Mass Transfer 101 (2016) 1138 – 1150. doi:https://doi.org/10.1016/j.ijheatmasstransfer.2016.05.108.
URL http://www.sciencedirect.com/science/article/pii/S0017931015313594

[18] C. Agrawal, R. Kumar, A. Gupta, B. Chatterjee, Rewetting and maximum surface heat flux during quenching of hot surface by round water jet impingement, International Journal of Heat and Mass Transfer 55 (17) (2012) 4772 – 4782. doi:https://doi.org/10.1016/j.ijheatmasstransfer.2012.04.045.

[19] C. Agrawal, R. Kumar, A. Gupta, B. Chatterjee, Effect of jet diameter on the maximum surface heat flux during quenching of hot surface, Nuclear Engineering and Design 265 (2013) 727 – 736. doi:https://doi.org/10.1016/j.nucengdes.2013.09.026.

[20] N. Karwa, P. Stephan, Experimental investigation of free-surface jet impingement quenching process, International Journal of Heat and Mass Transfer 64 (2013) 1118 – 1126. doi:https://doi.org/10.1016/j.ijheatmasstransfer.2013.05.014.

[21] H. Leocadio, J. C. Passos, A. F. C. Silva, Heat transfer behavior of a high temperature steel plate cooled by a subcooled impinging circular water jet, in: 7th ECI International Conference on Boiling Heat Transfer, 2009, pp. 1–7.

[22] H. Leocadio, C. W. M. van der Geld, J. C. Passos, Rewetting and boiling in jet impingement on high temperature steel surface, Physics of Fluids 30 (12) (2018) 122102. doi:https://doi.org/10.1063/1.5054870.

[23] H. Robidou, H. Auracher, P. Gardin, M. Lebouché, Controlled cooling of a hot plate with a water jet, Experimental Thermal and Fluid Science 26 (2) (2002) 123 – 129. doi:https://doi.org/10.1016/S0894-1777(02)00118-8.

[24] B. Wang, D. Lin, Q. Xie, Z. Wang, G. Wang, Heat transfer characteristics during jet impingement on a high-temperature plate surface, Applied Thermal Engineering 100 (2016) 902 – 910. doi:https://doi.org/10.1016/j.applthermaleng.2016.02.054.

[25] A. K. Mozumder, Y. Mitsutake, M. Monde, Subcooled water jet quenching phenomena for a high temperature rotating cylinder, International Journal of Heat and Mass Transfer 68 (2014) 466 – 478. doi:https://doi.org/10.1016/j.ijheatmasstransfer.2013.09.059.

[26] M. N. Õzişik, Heat Conduction, Wiley-Interscience publication, John Wiley & Sons, 1993.

[27] D. Maillet, S. André, J. C. Batsale, A. Degiovanni, C. Moyne, Thermal Quadrupoles: Solving the Heat Equation through Integral Transforms, John Wiley & Sons, 2000.

[28] H. Stehfest, Algorithm 368: Numerical inversion of laplace transforms [d5], Commun. ACM 13 (1) (1970) 47–49. doi:10.1145/361953.361969.

[29] J. V. Beck, B. Blackwell, C. R. St. Clair Jr., Inverse Heat Conduction: Ill-Posed Problems, Wiley-Interscience publication, John Wiley & Sons, 1985.

[30] F. S. Gunnerson, T. R. Yackle, Quenching and rewetting of nuclear fuel rods, Nuclear Technology 54 (1) (1981) 113–117. doi:https://doi.org/10.13182/NT81-A32759.

[31] V. V. Yagov, K. B. Minko, A. R. Zabirov, Two distinctly different modes of cooling high-temperature bodies in subcooled liquids, International Journal of Heat and Mass Transfer 167 (2021) 120838. doi:https://doi.org/10.1016/j.ijheatmasstransfer.2020.120838.

[32] G. Castanet, O. Caballina, W. Chaze, R. Collignon, F. Lemoine, The leidenfrost transition of water droplets impinging onto a superheated surface, International Journal of Heat and Mass Transfer 160 (2020) 120126. doi:https://doi.org/10.1016/j.ijheatmasstransfer.2020.120126.

[33] C. F. Gomez, C. W. M. van der Geld, J. G. M. Kuerten, R. Liew, M. Bsibsi, B. P. M. van Esch, The nature of boiling during rewetting of surfaces at temperatures exceeding the thermodynamic limit for water superheat, Journal of Fluid Mechanics 895 (2020) A3. doi:https://doi.org/10.1017/jfm.2020.232.

[34] M. Khavari, C. Sun, D. Lohse, T. Tran, Fingering patterns during droplet impact on heated surfaces, Soft Matter 11 (2015) 3298–3303. doi:http://dx.doi.org/10.1039/C4SM02878C.

[35] H. Ohtake, Y. Koizumi, Study on propagative collapse of a vapor film in film boiling (mechanism of vapor-film collapse at wall temperature above the thermodynamic limit of liquid superheat), International Journal of Heat and Mass Transfer 47 (8) (2004) 1965–1977. doi:https://doi.org/10.1016/j.ijheatmasstransfer.2003.09.020.

[36] K. Tsukamoto, Y. Kita, S. Inoue, T. Hamanosono, S. Hidaka, S. Ueoka, H. Fukuda, M. Kohno, Y. Takata, On the onset of quench during spray cooling: The significance of oxide layers, Applied Thermal Engineering 179 (2020) 115682. doi:https://doi.org/10.1016/j.applthermaleng.2020.115682.

[37] A. Labergue, M. Gradeck, F. Lemoine, Comparative study of the cooling of a hot temperature surface using sprays and liquid jets, International Journal of Heat and Mass Transfer 81 (2015) 889–900. doi:https://doi.org/10.1016/j.ijheatmasstransfer.2014.11.018.

[38] P. L. Woodfield, M. Monde, Estimation of uncertainty in an analytical inverse heat conduction solution, Experimental Heat Transfer 22 (3) (2009) 129–143. doi:https://doi.org/10.1080/08916150902805968.

[39] N. Hatta, J. ichi Kokado, K. Hanasaki, Numerical analysis of cooling characteristics for water bar, Transactions of the Iron and Steel Institute of Japan 23 (7) (1983) 555–564. doi:10.2355/isijinternational1966.23.555.

[40] M. Gradeck, J. Ouattara, B. Rémy, D. Maillet, Solution of an inverse problem in the Hankel space – infrared thermography applied to estimation of a transient cooling flux, Experimental Thermal and Fluid Science 36 (2012) 56–64. doi:https://doi.org/10.1016/j.expthermflusci.2011.08.003.

Appendix A. Validation of the inverse method

To calibrate the number of future time steps when using Beck's regularization method and to validate the inverse method used in this study, we performed an analytical two-dimensional simulation of the heat conduction within the heated plate. In this calculation, we considered an imposed heat flux on the heated plate's upper surface and insulated surface on the bottom one and on the two boundaries in the x-direction, and placed the thermocouples at the same positions found in the test sample in Fig. 3. The imposed heat flux has initially a Gaussian shape over the 7^{th} thermocouple (x_0), which is the jet impingement location, with a peak heat flux of $\varphi_{max} = 5$ MW/m^2, which is the same order found in the experiments. Then, the Gaussian shape (standard deviation $\sigma_\varphi = 20$ mm) was split in two parts moving in opposite senses on the x-axis at a velocity of $v_\varphi = 2$ mm/s, with an exponentially decreasing peak with a characteristic time $t_c = 60$ s. Explicitly, the equation used to generate the heat flux profile was:

$$\varphi(x,t) = \frac{\varphi_{max}}{2} \exp\left[0.5\left(\frac{x - x_0 \pm v_\varphi t}{\sigma_\varphi}\right)^2 - \frac{t}{t_c}\right] \tag{A.1}$$

This simulation generated values of the temperature evolution as if they were thermocouple measurements, which were noised by adding a random value to the temperature following a Gaussian distribution noise with zero mean and 0.2 $°C$ standard deviation (i.e. an independent and identically distributed noise). This noise is slightly larger than the observed one in our acquisition system condition (about 0.15 °C). After testing different number of future time steps, we found the optimal value $n_{fts} = 5$ that provided smooth values and without bias. Figure A.20 presents a comparison between the imposed heat flux profile in the simulation (represented by the lines) and estimated heat flux over the thermocouples' locations after inversion (represented by the symbols) at different moments. The imposed heat flux is well estimated between 280 and 520 mm, i.e. between the fourth and twelfth thermocouples, throughout the simulation, while large deviations are found outside this range. This is better visualized in Fig. A.21, comparing the imposed and estimated heat flux evolutions at different locations. At both limits considered fine for inversion (at 280 and 520 mm), there is an oscillation before the Gaussian heat flux passes over these locations; however, they do not affect the estimation of the heat flux raise, peak and decrease, which are the most important information during our experience. At 370 mm, the stagnation zone location, the peak heat flux is well estimated. We also presented two

examples of bad inversion at 220 and 580 mm, where the estimated values do not correspond at all with the imposed heat flux. Although all the temperature measurements are used to find the Fourier harmonics for the inverse method (as done in this validation process), we only used the estimated values between 280 and 520 mm in this study, where the inverse heat flux deviates from the imposed one, in average, by less than 0.05 MW/m^2.

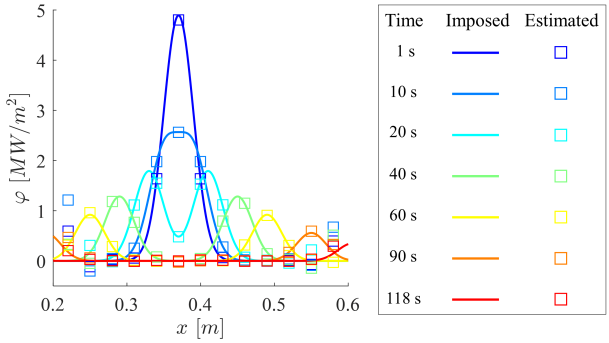

Figure A.20: Comparison between the imposed and estimated heat flux profiles at different times. The symbol's locations correspond to the thermocouples positions in the heated plate.

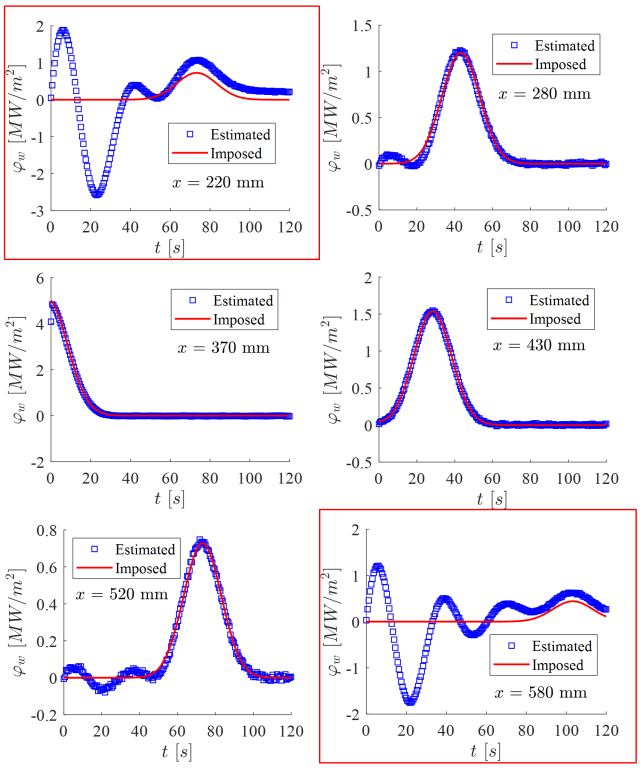

Figure A.21: Comparison between the imposed and estimated heat flux at different locations in the x-direction. Graphs highlighted in red are examples of bad inversion quality, therefore rejected in this study.

However, the inversion accuracy is affected by uncertainties in material properties, plate dimensions and thermocouples locations. For this reason, we performed a sensitivity analysis using Monte Carlo simulation to evaluate the effect of the thermophysical properties and the thermocouple depth uncertainties on the estimated heat flux. We considered the plate dimensions uncertainty negligible compared to these other effects. In this sensitivity analysis,

we used the imposed heat flux according to Eq. A.1 and the nominal values for the thermophysical properties and thermocouple depth. Then, we took the simulated temperatures to perform the inversion but, at this step, the material properties and the thermocouple depths were randomly varied following gaussian distribution with mean values corresponding to the their respective nominal values (given in section 3) and standard deviation of 10% for all the parameters. To collect enough data for a statistical analysis, we ran the simulation 20,000 times. Figure A.22 presents a histogram of the deviations $\Delta\varphi$ between estimated and simulated heat flux. This Monte Carlo simulation demonstrated that the uncertainties of the material properties and the thermocouples positions may lead to a slight bias in the heat flux estimation of about 0.08 MW/m^2, which is very low compared to the high heat fluxes observed during jet impingement cooling. Moreover, we can estimate the uncertainty of the inverse method as twice the standard deviation, i.e. 0.2 MW/m^2 with 95% confidence level.

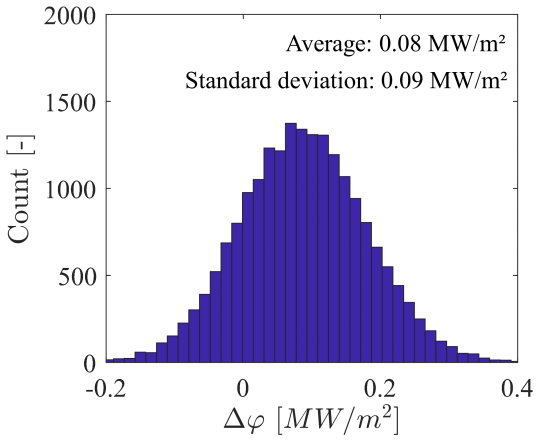

Figure A.22: Histogram of the deviations between imposed and estimated heat flux after a Monte Carlo simulation with 20,000 iterations (varying material properties and thermocouples depth from the cooled surface).